Further investigations into the accuracy of infrared-radiofluorescence (IR-RF) and its inter-comparison with infrared photoluminescence (IRPL) dating

Mariana Sontag-González[1], Madhav K. Murari[2], Mayank Jain[3], Marine Frouin[4], Markus Fuchs[1]

[1]Department of Geography, Justus Liebig University Giessen, 35390 Giessen, Germany
[2]Inter University Accelerator Centre, 110067, New Delhi, Delhi, India
[3]Luminescence Physics and Technologies, Department of Physics, Technical University of Denmark Risø Campus, Roskilde, Denmark
[4]Department of Geosciences, Stony Brook University, 255 Earth and Space Sciences Building, Stony Brook, NY 11794-2100, USA

Correspondence to: Mariana Sontag-González (Mariana.Sontag-Gonzalez@geogr.uni-giessen.de)

Abstract. Infrared radiofluorescence (IR-RF) is an alternative dating technique for potassium feldspar grains, offering a higher signal stability and based on a simpler underlying mechanism than more common luminescence dating approaches. However, its accuracy when tested on known-age samples has so far shown inconsistent results. In this study, we present a refined accuracy assessment using samples that have previously produced unreliable IR-RF ages. Our approach incorporates two major methodological advancements developed over the past decade: elevated temperature measurements using the IR-RF$_{70}$ protocol and sensitivity change correction by vertical sliding. To expand the dose range comparison, we included two additional samples: one expected to be in saturation and another of modern age. Additionally, we evaluated the effect of using a narrower bandpass filter to exclude any signal contributions from potentially contaminating shorter wavelength emissions. Our results following the IR-RF$_{70}$ protocol with sensitivity corrections show an improvement over the original room temperature results. For four out of the seven tested known-age samples spanning 20–130 ka, we obtained results in keeping with the expected doses. Two additional modern samples, however, yielded slight age underestimations. Introduction of a multiple-aliquot regenerative dose (MAR) protocol improved the accuracy of two out of three samples with large sensitivity changes. Finally, we also compared the new IR-RF equivalent doses (D_e) to those obtained with the newer trap-specific dating method infrared-photoluminescence (IRPL) for the same samples, including previously published values and new measurements. We observe that with the new improvements the success rate of IR-RF is comparable to that of IRPL.

1 Introduction

Infrared radiofluorescence (IR-RF) dating of potassium (K)-feldspar is a technique used to determine the time since sediment deposition (e.g., Trautmann et al., 1998, 1999; Erfurt and Krbetschek, 2003). The method consists of filling available electron

traps within the mineral's crystal lattice through continuous ionizing irradiation and quantifying the intensity of the resulting IR emission at ~880 nm (this emission was previously reported at 865 nm, see discussion in Sontag-González et al. (2022)). By comparing IR-RF curves obtained after natural burial with those obtained after a known laboratory dose (e.g., starting at zero dose following complete signal bleaching), the equivalent dose (D_e) accumulated since burial can be determined. Dividing

35 the D_e by the sample's environmental dose rate yields the time since burial. The main advantages of IR-RF dating over the more common infrared stimulated luminescence (IRSL) of K-feldspar (Hütt et al., 1988) include a more athermally stable signal (Krbetschek et al., 2000) and the large number of data points used to build the dose response curve (DRC).

Using a single-aliquot regenerative dose (SAR) protocol, Buylaert et al. (2012b) determined IR-RF ages for sixteen coarse-grained K-feldspar samples and reported poor agreement with the independent age controls, which ranged from modern

40 to ~130 ka. For three modern samples, the IR-RF D_e values were shown to be highly sensitive to the bleaching method used between natural and regenerative measurements, with the most accurate results obtained using a solar simulator bleach of at least 4 hours. The IR-RF ages of five young samples (~100–150 Gy) were overestimated by ~20–70%, while those of eight older samples (~200–300 Gy) were underestimated by ~20–40%. Over the past decade, significant methodological improvements in IR-RF dating have been developed, including measurement at 70°C instead of at room temperature (Frouin

45 et al., 2017) and a combination of horizontal and vertical sliding for D_e estimation (Kreutzer et al., 2017; Murari et al., 2018). The latter is intended to correct for reported sensitivity changes occurring between the two IR-RF measurements (e.g., Buylaert et al., 2012b; Varma et al., 2013). When introducing the IR-RF$_{70}$ protocol, Frouin et al. (2017) presented results for six samples, five of which matched the quartz-based ages (at 2σ). These new developments warrant a re-analysis of the previous findings on the accuracy of IR-RF ages reported by Buylaert et al. (2012b). Additionally, the segment of the natural dose curve used

50 for D_e estimation with a vertical slide analysis needs to be systematically investigated. Previous work using only a horizontal slide has shown that the D_e is sensitive to the length of the natural dose curve used for sliding (Frouin et al., 2017). It is also conventional procedure to reject initial channels to avoid the 'initial rise' effect, i.e., an unexpected signal increase at the beginning of natural and regenerative dose curves whose origin is not well understood (e.g., Buylaert et al., 2012b; Huot et al., 2015; Frouin et al., 2017). The initial rise has been shown to be dose-dependent (Frouin et al., 2017) and is avoided by removing

55 up to a few tens of Gy from the beginning of the natural dose curve. However, the extent of its effect on the D_e is still not clear.

In parallel, Prasad et al. (2017) proposed a new dating method for K-feldspar based on IR photoluminescence (IRPL), which is relevant in the context of IR-RF dating. Both methods involve the emission stemming from electrons relaxing from the excited to the ground state of the K-feldspar principal trap. In IR-RF, these electrons originate from the valence band and get trapped during the process, whereas, in IRPL, the electrons are already trapped but are stimulated to the excited state with

60 IR stimulation. Importantly, in IRPL, the electrons do not leave the trap, leading to a steady-state signal (i.e., electrons continuously 'bouncing' between the excited and ground states of the principal trap during IR stimulation) and thereby representing a non-destructive measurement technique. Kumar et al. (2018) identified two IRPL emissions resulting from stimulation with an 830 nm laser, which are centred at 880 and 955 nm (IRPL$_{880}$ and IRPL$_{955}$, respectively). They also demonstrated that these two IRPL emissions correspond to the two known IR-RF emissions and suggested that they arise from

65   the same defect (i.e., the principal trap) but with slightly different environments (i.e., neighbouring atoms or functional groups). The SAR IRPL protocol introduced by Kumar et al. (2021) also contains IRSL steps at increasing temperatures to sequentially target more stable traps, following the strategy of a multiple elevated temperature (MET) post-IR IRSL (pIRIR) protocol (Li and Li, 2011). Due to the non-destructive nature of IRPL, the inclusion of IRSL steps allows for the comparison of several IRSL and IRPL signals for the same aliquots. Of the eleven sediment samples dated with IRPL (Kumar et al., 2021), nine had

70   also been dated using IR-RF by Buylaert et al. (2012b). They observed good agreement between the IRPL ages and the independent age controls for eight samples ranging ~100–300 Gy, but obtained overestimated ages for three modern or very young samples. If the IRPL and IR-RF signals indeed originate from the same trap reservoir, they would be expected to yield similar D_e values, assuming there is no contamination from other emissions as well as negligible sensitivity changes during the measurement process. Kumar et al. (2021) observed poor agreement between their IRPL ages and IR-RF ages of the same

75   samples reported by Buylaert et al. (2012b), which were obtained using room temperature IR-RF measurements (IR-RF$_{RT}$), and without a correction for sensitivity changes. A comparison between IRPL measurements and the new improved IR-RF protocol (Frouin et al., 2017; Murari et al., 2018) are yet to be made.

        In addition, the upper dating limit of both IR-RF and IRPL are still poorly understood. In the case of IR-RF, previous studies suggest the onset of saturation of the natural signal at around 1000 Gy. This value is based on measurements of a

80   Triassic age sample expected to be in saturation (Murari et al., 2021), measurements of a sequence of known-age samples from the Chinese Loess Plateau (Buchanan et al., 2022), and a study of long-term signal stability using artificially-added gamma doses (Kreutzer et al., 2022a). These findings are at odds with the DRCs obtained in the laboratory, which continue to grow over >3000 Gy. The upper dating limit of IRPL has not been studied using natural samples yet. However, the characteristic saturation dose (85% saturation) of laboratory-irradiated DRCs ranges between ca. 1400 Gy and 2500 Gy (Kumar et al., 2021)

85   depending on the protocol used (e.g., with or without preheat). Comparison of the IRPL and IR-RF field-saturation doses will help determine whether the relatively low upper limit of ~1000 Gy for IR-RF dating is a characteristic of the principal trap (e.g., due to signal instability) or whether it is caused by IR-RF specific issues. One potential issue is an overlap of the targeted IR-RF emission (centred at 880 nm) with a neighbouring red emission, which has been reported to be thermally unstable (Krbetschek et al., 2000). This overlap can be problematic for D_e estimation by making the natural dose curve not directly

90   comparable to the regenerative dose curve, as the red signal would have already decayed in the natural sample but still contribute to the total signal in the regenerated dose curve. Spectroscopic measurements of a field-saturated sample by Sontag-González and Fuchs (2022) reported differences in mean D_e of ~400 Gy between integration of the dose ranges 810–850 nm and 850–890 nm, confirming that the detection window needs careful consideration. Shifting the detection window further into the IR reduces the contribution from the red emission, which we hypothesize would lead to more accurate D_e values.

95   Here, we re-analyse the original IR-RF$_{RT}$ data for the sixteen samples with independent age controls dated by Buylaert et al. (2012b) to include a sensitivity change correction (vertical slide) and present new IR-RF D_e values obtained using the IR-RF$_{70}$ protocol for eight of these samples, which are expected to be more accurate. The IR-RF$_{70}$ dataset was then expanded by including one additional modern sample and one sample expected to be in field-saturation (see Table 1 and Fig. S1). We

vary several IR-RF$_{70}$ measurement parameters to assess their effect on the resulting D$_e$ in an effort to determine the combination that leads to the most accurate results. Tested parameters include the use of the vertical slide, the type of bleach between the natural and regenerative dose curve measurements, the number of rejected initial channels, the length of the natural dose curve used for sliding, and the detection window. On the basis of the SAR results, which suggest large sensitivity changes occur during the natural dose measurement for some samples, we also test the suitability of an IR-RF multiple-aliquot regenerative dose (MAR) protocol. Finally, we compare the IR-RF$_{70}$ results with MET pIRIR-IRPL ages for ten samples. IRPL data of seven of these samples have been published by Kumar et al. (2021) and we measured three new samples.

2 Samples and methods

2.1 Sample selection and preparation

Eighteen samples (Table 1) were selected based on their independent age controls. Seventeen of these were prepared in the luminescence laboratory at Risø DTU following standard procedures. After initial wet-sieving, grain size fractions of 90–150, 90–180, 150–212, 180–250 or 150–250 µm in diameter were treated with 10% hydrogen chloride (HCl) and 10% hydrogen peroxide (H$_2$O$_2$) solutions to remove carbonates and organic matter, respectively. K-feldspar grains were then isolated using a heavy liquid solution with a density of 2.58 g/cm^3 and etched with hydrogen fluoride (HF; 10%) for 40 min to remove the alpha-irradiated outer layer. A final HCl treatment dissolved any contaminating fluorides. One additional sample, Gi326, was prepared in the luminescence laboratory in Giessen, using the same chemical treatments, except for HF-etching. This sample is from a Triassic sandstone and has been used previously to test the field saturation of IR-RF$_{70}$ (Murari et al., 2021).

Etching of K-feldspar has been reported to be uneven and sometimes lead to a larger volume removal than anticipated (Porat et al., 2015; Duval et al., 2018). The effect on the resulting D$_e$ is poorly studied, but since all samples expected to be in the dating range (i.e., not saturated) received the same treatment, we do not expect etching to affect our conclusions.

Due to a recently reported issue in past batches of the Risø calibration quartz (RCQ) commonly used to estimate the source dose rate (Autzen et al., 2022), we adjusted the expected D$_e$ of most samples. For the samples whose age controls were determined solely by quartz OSL (i.e., sample codes 075403, 075406, 075407, 072255, 055642, 102011, A8, and B12) we applied a correction factor of 8.25% (Autzen et al., 2022). We note that, in the original publications of samples from Gammelmark (Denmark) and Sula (Russia), the quartz OSL ages were reported to underestimate the expected Eemian age by ca. 7–15% (Murray and Funder, 2003; Murray et al., 2007). We interpret this observation as further support that the correction is necessary. For the eight samples from Gammelmark and Sula used here, we consider their expected ages to be 130 ± 2 ka (Murray and Funder, 2003; Murray et al., 2007), in contrast to the expected age of 128 ± 2 ka reported in Buylaert et al. (2012b) which presumably already accommodated the previous underestimated quartz OSL ages. The source dose rates for the data from Buylaert et al. (2012b) re-analysed here were also corrected by 8.25%.

2.2 Instrumental setup for IR-RF measurements

130 The original IR-RF$_{RT}$ luminescence measurements from Buylaert et al. (2012b) were obtained using a Risø TL/OSL DA-20 reader (Bøtter-Jensen et al., 2010) with a specific attachment (Lapp et al., 2012), where the signal is transmitted through an optical light-guide and filtered with a Chroma D900/100 interference filter before reaching a Hamamatsu H7421-50 photomultiplier tube (PMT). The effective detection window of this filter and PMT combination has a full width at half maximum (FWHM) spanning ~850–875 nm. Large aliquots (~8 mm), containing thousands of grains mounted on stainless

135 steel discs with silicone oil, were measured according to the IR-RF$_{RT}$ protocol outlined in Table 2. Aliquots were bleached between the natural and regenerative dose steps using either built-in UV LEDs (395 nm) or an external SOL2 solar simulator (Hönle AG).

New radiofluorescence measurements were performed at 70°C (IR-RF$_{70}$) using a *lexsyg research* device (Freiberg Instruments GmbH; Richter et al., 2013) in Giessen (Germany) equipped with an annular beta source ($^{90}Sr/^{90}Y$) calibrated with

140 a standard quartz sample using small aliquots on stainless-steel cups with silicone oil (RCQ batch 200; equivalent to 0.059 Gy/s on 01/01/2023). We assume an uncertainty of 5% for this calibration. Measurements in section 3.2 were all conducted at the University of Oxford (UK) on the same type of device; further details can be found in Sontag-González et al. (2024). The calibrated annular beta source had a dose rate of 0.053 Gy/s (01/01/2023). The radiofluorescence was filtered through a Chroma D850/40 interference filter before being detected by a Hamamatsu H7421-50 PMT with an effective detection FWHM

145 spanning ~825–860 nm. Additional experiments in section 4.5 tested a different interference filter centred at 880 nm with an FWHM spanning ~875–885 nm (Quantum Design 880HC10). Medium-sized aliquots (~3–4 mm), containing hundreds of coarse grains, were mounted on stainless steel cups with silicone oil. For the 'single-grain' measurements in section 3.2, an individual grain was manually placed on each sample holder and fixed with silicone oil. The new measurements followed the IR-RF$_{70}$ protocol outlined in Table 2. Aliquots were bleached using a built-in LED-based solar simulator, according to the

150 relative intensities in Frouin et al. (2015) and using the following power output: 365 nm (9 mW), 462 nm (55 mW), 525 nm (47 mW), 590 nm (32 mW), 625 nm (100 mW), and 850 nm (84 mW). In a separate bleaching test, some aliquots were bleached by direct sunlight exposure (see section 4.3).

2.3 IR-RF data analysis

Data analysis of both the previous and the new IR-RF measurements was conducted in an R programming environment v4.0.2

155 (R Core Team, 2020). D$_e$ values were obtained for each aliquot by sliding the 'natural dose' curves onto the 'regenerative dose' curves using either only a horizontal slide or both horizontal and vertical slides utilizing the function 'analyse_IRSAR.RF' from the 'Luminescence' (v0.9.19) package (Kreutzer et al., 2012, 2022b). The IR-RF$_{70}$ curves from a representative aliquot are shown in Fig. 1, where the extent of vertical and horizontal sliding of the natural dose curve is shown as red bars. Sample D$_e$ values were calculated using the arithmetic mean of the aliquot D$_e$ values and stated uncertainties are

160 the standard error of the mean with the source calibration uncertainty added in quadrature. In the few cases in which the

standard error was below the channel length (10 s, approximately 0.6 Gy), we considered the channel length as the mean D_e uncertainty because that is the limit of our resolution. Example D_e distributions are shown in Fig. S2.

Following conventional procedure, the initial channels of each natural measurement were ignored during the analysis to account for the initial rise. The initial rise phenomenon is apparent in the first few data points of the curves shown in Fig. 1; in this case, removing the first channel of the natural dose curve would be sufficient to make the natural and regenerative dose curves comparable over the dose range of interest. We tested different rejection lengths, ignoring between 0 (no rejection) and ~300 Gy of the initial part of the natural dose curve (i.e., removing between 0 and 499 channels). The effect of rejecting initial channels will be detailed in section 4.4.

2.4 IRPL equipment and procedure

We measured the IRPL emissions centred at 880 and 955 nm for three samples using the same equipment as Kumar et al. (2021), including a $^{90}Sr/^{90}Y$ beta source calibrated using small RCQ aliquots on stainless-steel discs (equivalent to 0.19 Gy/s on 01/01/2023). We used the IRPL attachment (Kook et al., 2018) to the Risø TL/OSL reader with two photomultiplier tubes: a Hamamatsu H10330C-25 in combination with a bandpass interference filter centred at 950 (FWHM of 50 nm) for the $IRPL_{955}$ emission and a Hamamatsu H7421-50 in combination with either a bandpass interference filter centred at 880 nm (FWHM of 10 nm) for the $IRPL_{880}$ or BG39 and BG3 filters for the IRSL emission. IR LEDs (850 nm with a power density of ~250 mW/cm^2 at sample position) were used as the stimulation for IRSL. The IRPL stimulation consisted of an external laser light source (830 nm with a power density of ~3 mW/cm^2 at sample position) in a pulsed excitation mode (50 µs on-time followed by 50 µs off-time) for 5 s. IRPL was only measured during the off-time, rejecting the first 3 µs to avoid contamination by the excitation source (PMT gate 53–100 µm).

The measurement protocol consists of an MET pIRIR protocol based on Protocol A of Kumar et al. (2021) and using IR stimulation temperatures of 50°C, 90°C, 130°C and 290°C ($IRSL_{50}$, $pIRIR_{90}$, $pIRIR_{130}$, $pIRIR_{290}$, respectively) with room temperature IRPL measurements interspersed between each step (Table S1). The preheat step was set to 320°C (60 s) and the IR stimulation at 290°C (100 s) was used to remove residual signal prior to each irradiation step (cleanout). IRPL signals for each emission were calculated as the integral of the 5 s long measurements, subtracting as background the residual IRPL obtained after the 290°C IR cleanout (step 16 or 17 in Table S1 for $IRPL_{880}$ or $IRPL_{955}$, respectively). Fig. S3 and Fig. S4 show examples of the IRPL curves used to obtain the signal and background, respectively. Fig. S5 displays examples of the resulting DRC. IRSL signals were also determined for comparison, consisting of the integral of the first 2 s with the last 10 s used for background subtraction. Sensitivity change corrections for IRSL and IRPL consisted of dividing the signal obtained from the natural or various doses (L_n or L_x, respectively) by that obtained from a test dose (T_n or T_x) for each SAR cycle. The IRPL and IRSL DRCs were fitted with double exponential functions for better comparability with Kumar et al. (2021). Aliquots were only considered for D_e estimation if they passed the following criteria: minimum signal brightness (T_n more than three sigma of the background level and a relative standard error of T_n <10%), reproducibility (recycling ratio within 10% of unity) and low signal carry-over (recuperation <15%).

3 Considerations on the IR-RF DRC

195   Among other parameters, in section 4, we will investigate the segment of the natural dose curve that should be used for D_e estimation with a vertical slide analysis. In theory, if the natural and regenerative dose curves have the same signal components and follow the same decay, we would not expect any difference in D_e values from natural dose curves of different length, provided the segment is long enough for a statistically reliable slide. We can test this hypothesis by measuring a long natural dose curve for all aliquots and repeating the D_e analysis using segments of different lengths. Two parameters can be changed

200   in this analysis: the start and the end channels of the natural dose curve segment to be used for sliding. Since our natural dose curves are composed of 3000 channels (~1800 Gy), we have over 4 million possible segments (assuming the segment should be at least 2 channels long). Naturally, not every combination makes sense, so here we summarize past studies and preliminary analyses to inform on the combinations we should focus on.

3.1 Initial signal rise: removing initial channels

205   The segment of the natural dose curve visibly affected by the initial signal rise is often avoided for dating. For example, Buylaert et al. (2012b) removed between 1 Gy and 33 Gy from the start of the curve. Frouin et al. (2017) reported a dose-dependence of the initial rise, with the peak maximum ranging from ~2 Gy to ~40 Gy for samples with D_e values of 0 Gy to ~300 Gy. Similar values were reported by Murari et al. (2021): ~3 Gy and ~20 Gy for a modern and a saturated sample, respectively. Thus, removal of up to the initial ~40 Gy appears to be warranted.

3.2 Initial signal rise: insights from single-grains

210   Previous research has suggested differences in IR-RF characteristics at the single-grain level which would be averaged in the multi-grain aliquots used in the present work (Trautmann et al., 2000; Frouin et al., 2017; Mittelstraß and Kreutzer, 2021). For example, our earlier work on sample H22550 (Sontag-González et al., 2024) revealed that only three out of six measured grains produced the expected IR-RF signal (i.e., decreasing with dose, referred to as Type #1). One additional grain exhibited an

215   initial signal rise followed by signal saturation at ~100 Gy (termed Type #2). The remaining two grains showed a flat signal shape indistinguishable from that of an empty sample holder. These results suggest potential issues for multi-grain measurements. By mathematically adding the IR-RF signal (i.e., a synthetic aliquot) obtained from individual grains of sample H22550 by Sontag-González et al. (2024), we modelled the signal from multi-grain aliquots with different proportions of the two grain types (Fig. 2). If at least one third of the grains in a multi-grain aliquot yield the expected IR-RF signal, they will

220   dominate the total signal and, overall, the signal shape will follow the Type #1 grain pattern (Fig. 2, inset). Interestingly, our modelled signal displays an 'initial signal rise' which decreases with a decrease of the proportion of unwanted Type #2 grains. This suggests that (i) the 'initial signal rise' originates from signal contamination by presumably non-K-feldspar minerals and (ii) the signal shape at doses higher than ~100 Gy is not significantly compromised by this phenomenon. This observation suggests we should investigate removing a larger portion of the initial curve than previously expected.

3.3 Length of natural dose curve segment

Frouin et al. (2017) conducted an iterative test increasing the segment length over the first 100 channels (horizontal slide) and found that for their samples a D_e plateau was reached after ~40 channels (~30 Gy with their 0.7 Gy/channel). In Buylaert et al. (2012b), the natural dose curve length varied between 5 and 475 Gy, depending on the sample. More recent studies are showing a preference for the use of long natural dose curves of ~260 Gy (Key et al., 2022) or 500–600 Gy (Murari et al., 2021; Scerri et al., 2021; Kreutzer et al., 2022a; Buchanan et al., 2022, 2024).

For a preliminary analysis, we tested the effect of varying the natural dose curve segment for one sample (981009). Having measured long curves of ~1800 Gy, we obtained 2996 mean D_e values using incrementally larger segments (Fig. 3), having removed the initial ~2 Gy (4 channels) in all iterations. When using the vertical and horizontal analysis, a large change in D_e values was observed (Fig. 3b) but no D_e plateau was reached. Short segments (< 15 Gy) led to unrealistically high D_e values of thousands of Gy possibly due to the uncertainties of the sliding algorithm, so we will focus on larger curve segments. Six representative segment lengths of between ca. 75 Gy and 1800 Gy were chosen to cover the range expected to yield reliable results for dating.

4 IR-RF D_e estimation

4.1 Effect of vertical slide correction

The original mean D_e values obtained by Buylaert et al. (2012b) using an IR-RF$_{RT}$ protocol are reproduced in Fig. 4a (open circles). When using the internal UV LEDs for the bleaching steps between the natural and regenerative dose steps, the D_e values are either over- or underestimated (at 2σ) for all sixteen samples. By replacing the UV bleaching step with an external bleach in a solar simulator (SOL2) for a subset of six samples, Buylaert et al. (2012b) observed an improvement in results, but the D_e values were still under- or overestimated for five of the six samples tested (Fig. 4a, open squares).

Application of the new vertical slide correction for sensitivity changes led to an increase in D_e values for all samples except for one of the modern ones (Table 3 and Fig. 4a, filled symbols). This adjustment resulted in eight samples aligning with the expected D_e (at 2σ), but it also increased the overestimation for most of the other samples. A similar pattern was observed for the aliquots bleached with UV LEDs and with SOL2. For the UV LED dataset, the sensitivity change correction led to an increase in the scatter of the D_e distribution of most samples, evident from the increased standard errors of the mean (Fig. 4a). These results suggest that sensitivity change corrections alone do not improve the accuracy of IR-RF$_{RT}$ results.

4.2 Effect of measurement temperature

Of the sixteen samples analysed in section 4.1, we selected eight for new measurements at 70°C, keeping only 1–2 samples per site. The new measurements using the IR-RF$_{70}$ protocol showed a better agreement with the expected values (Fig. 4b).

Four of the samples have D_e values matching expectations at 1σ. Interestingly, for these four samples, results with and without the sensitivity change correction were indistinguishable from each other at 1σ.

For all aliquots, we measured the natural dose curves over a relatively long dose range of ~1800 Gy when using the IR-RF$_{70}$ protocol. However, for the results shown in Fig. 4a–b we used the same dose ranges in the sliding procedure as in the original analysis of Buylaert et al. (2012b) to allow for a more direct comparison. We adjusted the total lengths of the natural dose curve segments (5–475 Gy) and removed the initial channels (1–33 Gy) aliquot-wise.

4.3 Effect of type bleaching type

Given the large differences in IR-RF D_e observed by Buylaert et al. (2012b) when using the internal UV LEDs or an external solar simulator (SOL2) for the signal bleach between the natural and regenerative dose steps, we tested the efficacy of the internal solar simulator for IR-RF$_{70}$ measurements by comparing it to a solar bleach. We used three samples with poor matches to their expected doses (sample No. 092202, 075406 and 072255) and one sample that matched its expected dose (H22553). Three aliquots per sample received an external solar bleach between the natural and regenerative steps by placing them on a windowsill for one week in late May in Giessen, Germany. The aliquots were exposed to cumulative ~82 h of daylight, including at least 8 h of direct sunlight. For three of the four samples, D_e values obtained with vertical slide correction were statistically indistinguishable (at 1σ) from those obtained using the internal solar simulator (Fig. 4b), suggesting that the type of bleaching may contribute to the inaccuracy of some samples, but is not the main cause behind it.

4.4 Sliding range of IR-RF$_{70}$ natural dose curve

Now, we will investigate how the choice of the natural dose curve segment used for sliding affects the resulting D_e value with the IR-RF$_{70}$ protocol following the considerations laid out in section 3. For the following, we added two new samples to the dataset, which were not analysed by Buylaert et al. (2012b): a modern sample (B12) and a field-saturated sample (Gi326). At least three aliquots were measured per sample.

First, we assessed the dose range that should be removed from the beginning of the natural dose curves to mitigate the initial rise effect. We compared the mean D_e values resulting from using the initial ~150 Gy of the natural dose curve, while rejecting various initial amounts: 0 (no rejection), 2, 5, 11, 17, 36 or 72 Gy for each of ten samples (Fig. 5a–b). Note that the rejected channels are still considered for D_e calculation as laboratory-added dose even though they are excluded from the sliding algorithm to assess goodness-of-fit. Using only a horizontal slide analysis (Fig. 5a), we observed no significant change in D_e except for the modern samples, for which only the iterations without any rejection matched the expected doses. When applying the sensitivity change correction (Fig. 5b), we observed a pattern of gradual decrease in D_e values of up to 17% (relative to the no rejection scenario) for all non-modern samples.

We then repeated this test using longer segments of the natural dose curve (~300 Gy or ~600 Gy) while rejecting the initial 0–150 Gy or 0–301 Gy for each of the ten samples (Fig. 5c–d and 5e–f, respectively). Similar patterns as with the short

segment were observed but with a smaller gradual change in D_e with increasing segment length for the non-modern samples (up to 10% and 11% relative to the no rejection scenario, respectively). Comparing results from natural dose curve segments of different lengths (~150, 300 or 600 Gy) with sensitivity change correction (Fig. 5b, 5d and 3f, respectively) reveals that the length of the segment has a higher impact on D_e than the amount of rejected initial channels. If the natural dose curve is sufficiently long, up to ~35–100 Gy can be removed to address the initial rise effect.

However, the question remains as to how long the natural dose curve should be. We tested this by fixing the beginning of the curve (rejecting the initial 2 Gy to avoid the channels most affected by the initial rise) and changing the length of the curve to span ~75, 150, 300, 600, 1200 or 1800 Gy, i.e., 125, 250, 500, 1000, 2000, or 3000 channels, respectively (Fig. 5g– h). For the two modern samples, we observed minimal D_e variation. For the other samples and without a sensitivity change correction, we observed a gradual increase in D_e with increasing length of the natural dose curve (Fig. 5g). Relative to the shortest segment (~75 Gy), the D_e values increase by between 3% and 27% with the larger increases (15–27%) observed for the field-saturated sample and for the three samples with poor matches to the expected doses. Note that for the field-saturated sample, the longest segment yielded only a minimum dose estimate due to the limit of the regenerative dose curve (i.e., the analysis algorithm restricts sliding the natural dose curve further than the end of the regenerative dose curve). The remaining four samples showed only 3–5% increase. We observed a similar pattern when applying the sensitivity change correction, but the trend of increase in D_e generally begins only for segments >300 Gy and it is superimposed onto an initial D_e decrease (see also Fig. 2b).

The results shown in Fig. 5g–h suggest sensitivity changes occur during measurement of the natural dose curve that are not corrected by vertical sliding, as this method only addresses changes between the end of the natural and beginning of the regenerative dose curves. A comparison of the fit quality between the natural and regenerative dose curves for samples with small and large sensitivity changes is shown in Fig. S6.

To further investigate sensitivity changes, we repeated the D_e estimations for all samples using segments of the natural dose curves spanning ~300 Gy, but beginning at either 2, 301, 602, 903, 1205 or 1506 Gy (Fig. 5i–j). We observed a gradual change in D_e for all samples with both analysis types. Without a sensitivity change correction, D_e values increased by up to 22–294% (relative to the initial segment) for the non-modern samples. The three samples whose D_e values consistently overestimate (sample No. 092202, 075406 and 072255) had much larger increases (78–294%) than the four other non-modern samples (22–36%). The modern samples had either an increase or a decrease of 60–75 Gy. For the field-saturated sample, the final three segments yielded only a minimum dose estimate due to the limit of the regenerative dose curve. We observed a D_e increase of up to 32% for the field-saturated sample but expect that that number would be higher if the regenerative dose curve had been longer and thus allowed for an absolute value for the final three segments. With the sensitivity change correction, the D_e increases were less pronounced: up to 49–116% for the three 'problematic' samples as well as the field-saturated sample and up to 12–28% for the other non-modern samples.

Overall, the length of the natural dose curve segment used for sliding affects the resulting D_e values for most of the tested samples. For short segments (e.g., ≤151 Gy), results using the vertical slide analysis are very sensitive to an initial

320 channel rejection. Excessively long segments might lead to a dose overestimation possibly due to sensitivity changes occurring during the natural dose curve measurement. A segment of ~300 Gy seems to be relatively insensitive to the rejection of the initial channels for non-modern samples and avoids the D_e increase observed for longer segments. Mean D_e values for all samples using this segment are given in Table 4 and shown in Fig. 4c (see Fig. S2 for the D_e distributions).

4.5 Detection window

325 The observed dose-dependent mismatch between the natural and the regenerative dose curves could be due to varying contributions from neighbouring emissions to the total signal. To test whether the observed D_e variations are caused by a contribution of the red RF emission (centred at ca. 700–730 nm; Trautmann et al., 1998; Krbetschek et al., 2000), we shifted the detection window further into the IR by replacing the bandpass filter centred at 850 nm (FWHM: 40 nm) with one centred at 880 (FWHM: 10 nm) and repeating all measurements (three aliquots per sample) and analyses discussed in section 4.4. We

330 chose a filter with a narrower detection window to avoid emissions in shorter or longer wavelengths than the desired 880 nm RF emission. If the red emission contributed to the total signal, we would expect a higher D_e accuracy and lower D_e variations with segment choice when using the new filter.

Measurements with the 880 nm filter showed slightly more variability, probably due to the lower signal intensity with the narrower filter (compare Fig. S6 and S7). However, we generally observed similar patterns with both filters. The mean D_e

335 values are statistically indistinguishable (at 2σ) for nine of the ten samples. An overview of the results for all tested natural dose segments is shown in Fig. S8. The mean IR-RF$_{70}$ D_e values for all samples using the initial ~300 Gy segments are given in Table 4 and compared with those using the broader filter in Fig. 4c (the results for sample Gi326 will be discussed in section 7).

5 An IR-RF MAR protocol

340 As indicated in section 4.4, some samples appear to suffer from significant progressive sensitivity changes during the first laboratory irradiation, thereby making the natural and regenerative dose curves not directly comparable. More importantly, the vertical slide is not an effective technique to correct for such progressive sensitivity changes, as it only corrects for changes in signal intensity but still assumes that the curve shapes are comparable. In luminescence dating, MAR procedures (Aitken, 1998) can be implemented to circumvent sensitivity changes when the typical test dose correction in a SAR protocol is deemed

345 insufficient for either quartz (e.g., Lu et al., 2007; Ankjærgaard, 2019) or K-feldspar applications (e.g., Li et al., 2013). In MAR protocols, the natural and regenerative data sets stem from different aliquots, with the latter being bleached to remove the natural signal prior to a laboratory irradiation.

We tested the suitability of an IR-RF MAR protocol to overcome the sensitivity changes induced by the first laboratory irradiation of an aliquot. The protocol consisted of obtaining the natural dose curves for several aliquots following

350 the same steps as in a SAR protocol (for simplification, the same dataset was used as in section 4.4), whereas the regenerative

dose curves (one per sample) were obtained from new aliquots in which the natural dose curve step and associated preheat were skipped (MAR protocol in Table 2). To account for inter-aliquot differences in mass and signal intensity, each SAR natural dose curve was scaled by the ratio between the first data point of the MAR and SAR regenerative dose curves, as exemplified in Fig. S9. An instrumental background was subtracted from each curve prior to normalisation, using the mean signal intensity of a 1000 s long measurement of an empty sample holder (12 961 cts/channel).

We repeated the MAR D_e analysis using varying natural dose curve segments, as previously described for the SAR protocol in section 4.4. As shown in Fig. S10, use of different segments led to different D_e values for all ten investigated samples, though some differences in pattern are of note. Unlike the SAR analysis, in which use of an increasingly long natural dose curve segment led to higher D_e values for all samples (Fig. 5h), with the MAR analysis, increasingly long segments (i.e., 2−151 Gy to 2−1808 Gy) led to a better agreement with expected D_e values for five non-modern samples and very small changes for the remaining four samples of known age (Fig. S10d). For this reason, we also considered how many channels should be removed from the beginning of the 1808 Gy-long natural dose curve (Fig. S10c). We found that rejecting the initial 108 Gy was the best compromise to achieve a good agreement with expected D_e values across the non-modern samples (Fig. 6a and Table 4). The MAR protocol using a natural dose curve segment of 108−1808 Gy (180−3000 channels) with vertical and horizontal slide yielded D_e in agreement with the expected values (at 2σ) for five out of the seven non-modern samples of known age, including for two of the three samples identified as 'problematic' in section 4.4.

6 Comparison of IR-RF and IRPL

A subset of the samples used in section 4 to evaluate different IR-RF protocols have also been used to assess the accuracy of IRPL (Kumar et al., 2021), allowing us to directly compare both methods. To create a more comprehensive dataset, we measured three additional samples (075406, A8 and Gi326) following an IRPL protocol and using the same equipment as Kumar et al. (2021). For each sample, between three and seven aliquots were measured.

Since the IRPL signal measurement is mostly non-destructive, it can be taken at several steps in the protocol, yielding several IRPL D_e values for each emission (i.e., both before and after the preheat as well as after each IRSL step). Note that the IRPL steps after the $IRSL_{290}$ step are merely used to determine a background signal (see Fig. S4) and do not yield a D_e value. In this study, we measured the 880 nm and the 955 nm IRPL emissions. The sequential IRSL steps can also each be used to obtain a D_e value, thus resulting in a total of fourteen D_e values for each aliquot (see Table S1).

The mean D_e value for each IRPL signal of the field-saturated sample Gi326 is shown in Fig. 7a. With the exception of the $IRSL_{50}$ D_e, which is expected to be significantly affected by fading, all other D_e values are similar, ranging from ~1100 to ~1400 Gy. After the $IRSL_{50}$ step, we observed a convergence of the different IRPL signals to ~1200 Gy. This value is slightly lower than the $pIRIR_{290}$ mean D_e value at 1293 ± 14 Gy (Fig. 7a) and the IR-RF mean sensitivity change corrected D_e values, which are also at ~1300 Gy (Fig. 7b–d). We do not notice a significant change between the $pIR_{50}IRPL$ and the following IRPL mean D_e values, suggesting there is no sequential removal of unstable IRPL signal after increasingly hot IRSL steps

beyond 50°C for this sample. A similar behaviour is observed for the three pIRIR mean D_e values, though the large uncertainties in the $pIRIR_{90}$ and $pIRIR_{130}$ mean D_e values might obscure the expected step-wise increase in signal stability with

385   increasing IRSL temperature (e.g., Li et al., 2013).

       Kumar et al. (2021) stated that the $IRPL_{880}$ after the preheat step ($APh\text{-}IRPL_{880}$) and the $pIR_{50}IRPL_{955}$ signals are the most promising ones for sediment dating, based on a better agreement with the expected doses. Mean D_e values for these two signals, including two new samples are shown in Fig. 6b together with the most promising IR-RF signal. The values for other IRPL signals are shown in Fig. S11 (new samples) and Fig. S12 (all samples). The mean D_e values from the $pIR_{50}IRPL_{955}$

390   signal in Fig. 6b are in good agreement (at 2σ) with the expected doses for all non-modern samples and for six out of seven samples using the $APh\text{-}IRPL_{880}$ signal including two samples strongly overestimated with $IR\text{-}RF_{70}$. However, $IR\text{-}RF_{70}$ is in much better agreement than any of the IRPL signals for the two modern samples. See Fig. S13 for a direct comparison of the IR-RF and IRPL D_e values.

7 DRC shape and signal saturation

395   The results presented in section 4 showed variability in the $IR\text{-}RF_{70}$ signal across samples regarding their potential to yield the expected dose and the purported sensitivity changes occurring during the natural dose curve measurement. To assess the variability of the IR-RF curve shapes, we plotted all curves obtained with the 850 nm bandpass filter (FWHM: 40 nm) in Fig. 8. In the natural dose curves (Fig. 8a), the modern and field-saturated samples are distinguishable by their steeper and flatter shapes, respectively (highlighted in pink and grey, respectively). The regenerative dose curves (Fig. 8b) show sample-

400   dependent variability in signal brightness and in the 'background' level after ~4000 Gy. However, after subtracting the signal value at 1800 Gy as background and normalising the natural dose curves to the signal value at 3 Gy (to discount patterns caused by the initial signal rise), the natural DRC shapes of all samples are relatively similar (Fig. 8a, inset), with small differences observed for the field-saturated and modern samples as well as for samples 092202 and 075406. In contrast, an equivalent analysis of the regenerative dose curves yielded larger differences in DRC shape (Fig. 8b, inset). All samples follow

405   a similar pattern, except for samples 092202 and 075406 (highlighted in blue and orange in Fig. 8), which saturate later and earlier than the other eight samples, respectively. These two samples were also identified as problematic in section 4.4 when using different segments of the natural dose curve for sliding. An early-saturating DRC could potentially explain gradually more inaccurate D_e values (as observed in Fig. 5i−j) due to the higher uncertainties when using a flatter curve for sliding (i.e., near saturation). However, the same behaviour of gradually higher overestimation was observed for sample 092202 with a

410   late-saturating curve and for sample 072255, whose curve shape follows the consensus. Thus, variability in saturation behaviour does not seem to be the root cause of the observed D_e inaccuracy. The shapes of the MAR DRCs (in Fig. 8c) follow the same overall pattern across samples as the regenerative dose SAR curves.

       We also compared the $IR\text{-}RF_{70}$, -IRPL and pIRIR DRC shapes up to ~4000 Gy for representative aliquots of the field-saturated sample Gi326 (Fig. 9). Note that only the $pIR_{50}IRPL_{955}$ signal is shown in Fig. 9, but all IRPL signals measured after

415   the preheat step have very similar DRC shapes (see Fig. S5). Likewise, the IR-RF$_{70}$ DRCs of sample Gi326 measured with an 880 nm (FWHM: 10 nm) or an 850 nm (40nm) bandpass filter are very similar in shape (compare Fig. S6 and Fig. S7). By plotting the regenerative IR-RF curves onto an inverted axis, we could directly compare their shapes to those of the other signals, despite their decrease with increasing dose. To assess only the dynamic range of the IR-RF curve, we accounted for the high background signal typical of IR-RF by subtracting the median signal of the last 100 channels (~60 Gy) from all data

420   points. The curves were then normalised to their maximum signal values. The DRC behaviour is quite similar for all three signals using SAR protocols. None of the three signals seems to provide a significant advantage in terms of onset of signal saturation and thereby an extension of the datable age range. The mean D$_e$ values obtained with IR-RF, IRPL and pIRIR in sections 4, 5 and 6 (summarized in Fig. 7) suggest an upper limit of 1000–1300 Gy for these signals. By vertically projecting the mean D$_e$ of each signal onto the corresponding curve, we can qualitatively assess the percentage of signal saturation.

425   Assuming the signals do not continue to grow past 4000 Gy, field-saturation was achieved at ~80–85% saturation in all three SAR-based curves; the MAR IR-RF field-saturation was slightly higher at 87−89%. If the curves had been continued until full signal saturation, the percentages would be slightly lower. These results suggest a similar small long-term signal instability for the three emissions in this sample.

8 Discussion

430   In the present work, we re-analysed the IR-RF$_{RT}$ data of sixteen samples previously examined by Buylaert et al. (2012b) using an updated data analysis method for D$_e$ estimation known as vertical slide correction. This technique accounts for sensitivity changes occurring between the natural and regenerative dose curve measurements. Application of this correction method improved the accuracy for half of the samples but led to overestimations for most of the other half (see Fig. 4a and Table 3).

     We also re-measured eight of these samples with a newer and modified measurement protocol and included two

435   additional samples of known age to expand the dataset for a following comparison with IRPL. Our new measurements differed from the original ones in three main aspects: the measurement temperature, the length of the natural dose curve measurement and the detection window. Measuring RF at an elevated temperature to keep the shallow traps empty following the IR-RF$_{70}$ protocol (Frouin et al., 2017) had a large impact on D$_e$ and, hence, on improving the accuracy of the resulting ages (see Fig. 4b). The temperature of 70°C was suggested by Huot et al. (2015), corresponding to the temperature at which shallow traps

440   are empty and also the temperature spontaneously reached by the thermocouple during the bleaching step in their *lexsyg* research device. This temperature was then implemented and tested in Frouin et al. (2017) based on a series of IR-RF measurements of nine samples. As new devices have been developed and given the temperature sensitivity of K-feldspar signals, users should conduct systematic IR-RF tests (e.g., dose recovery) to assess the protocol parameters for their samples.

     Determining the optimal length of the natural dose curve used for sliding is challenging. In Buylaert et al. (2012b),

445   the natural dose curve length varied between 5 and 475 Gy, depending on the sample. Contrary to our expectations, we observed continuing changes in mean D$_e$ values when varying the natural dose curve length from ~75 to ~1800 Gy (Fig. 5g

and h). It is important that the segment not be too short to ensure a good comparison between the natural and regenerative dose curves, especially when using the vertical slide. Here, we determined that a length of ~300 Gy for the natural dose curve yielded the most promising mean D_e values in a SAR protocol, representing the intersection between two behaviours, a D_e decrease possibly caused by the segment being too short for a reliable slide and a D_e increase possibly related to sensitivity changes, as summarized in Fig. 10a. However, we stress that we do not consider this to be the definitive segment length until the mechanism behind the changes in D_e is explained. As for the vertical slide sensitivity change correction, its application led only to a small difference in the mean D_e of the four samples that agreed with the expected doses (at 2σ) and the two modern samples. In contrast, for three samples, the vertical slide led to a significant change in D_e, but neither analysis version agreed with the expected doses (Fig. 4c). Nevertheless, we recommend always using the vertical slide correction, given that sensitivity changes are known to occur and can vary in extent for different samples (e.g., compare Fig. 5g and h).

We also recommend removing initial channels to avoid the initial rise in IR-RF signal seen in most measurements. The effect of initial channel removal is dependent on the length of the natural dose curve (compare Fig. 5b, d and f) and sample-specific characteristics. We observed no general improvement of accuracy when removing a large initial segment, e.g., ~100 Gy, as suggested by the modelling in section 3.2, so we recommend removing only the segments visually affected by the initial rise. Here, that corresponded to the initial ~2 Gy (4 channels). Using the SAR protocol on the two modern samples, such a rejection led to slight dose underestimations (resulting in chronologically impossible negative ages), whereas no rejection yielded mean D_e values of 0.0 ± 0.6 Gy for both samples, matching the expectation (at 2σ). Similar results were found for the MAR analysis. We expect that the sharp signal peak caused by the initial rise phenomenon biases the fitting algorithm towards 0 Gy, as the peaks of the natural and regenerative dose curves align. Therefore, we suggest that the better agreement without any rejection is merely coincidental in the case of the modern samples since the initial rise is always at the beginning of the curves and maintain that some initial channels should be rejected. Further work would be needed on low-dose samples to explain the observed underestimation and assess the best number of rejected initial channels. However, at this stage, we caution against the reliability of IR-RF D_e values below ~100 Gy, due to the possible interference from other RF emissions (see section 3.2).

Returning to the non-modern samples, the only common feature among the three samples with SAR D_e values that did not match expected doses was a large increase in D_e (49–116%, with a vertical slide) when using progressively higher-dose segments of the natural dose curve for sliding (Fig. 5j). The D_e increase of the four other non-modern samples was much lower (12–28%), indicating lower sensitivity changes. We, therefore, tentatively propose using this characteristic as a screening tool to select samples that can be reliably dated by a SAR IR-RF protocol. Based on the current samples ranging ~100−300 Gy, a threshold of 35% in D_e increase of the final dose segment (~1500−1800 Gy) relative to the initial dose segment (~2−300 Gy) would separate the two groups (Fig. 10b). Use of a MAR protocol succeeded in obtaining D_e values compatible with the expected doses for two of the three samples with large progressive sensitivity changes (see Fig. 6a).

We also compared two IR-RF$_{70}$ detection windows (~825–860 nm and ~875–885 nm). In theory, a detection window further into the IR would be advisable by being less prone to contamination from a red emission. However, for the present

samples, no significant accuracy improvement was observed (see Fig. 4c), suggesting that the sensitivity changes occurring during the natural dose curve measurement are not caused by an overlay of an unstable emission. However, the existence of other emissions (or non-radiative recombinations) could be responsible for additional sensitivity changes by altering the proportion of electrons available for the IR-RF process, i.e., through competition effects. Such effects would be present at any detection window of the IR-RF signal. Our findings directly support the comparability of the new IR-RF results with those that would have been obtained with a Risø system, whose standard IR-RF filter has an effective detection window spanning 850–875 nm. A previous IR-RF$_{70}$ laboratory comparison that included both systems also supports their comparability, having yielded D$_e$ values matching at 1σ (Murari et al., 2021).

Our comparison of IR-RF$_{70}$ and IRPL results indicated some interesting differences and similarities between the methods. Whatever causes the overestimation of ~25–70 Gy in the IRPL signals for the two modern samples does not seem to affect the IR-RF$_{70}$ signal, despite our understanding that the same trap populations are being accessed. Inversely, the large overestimation of three samples with IR-RF$_{70}$ in the expected dose range 100–160 Gy was not observed for any of the IRPL signals, which yielded D$_e$ values not only closer to the expected doses, but depending on the IRPL signal (see Fig. S12) even matching the expectations (at 1σ). Nevertheless, we also highlight that only one IRPL protocol was tested (i.e., a high-temperature SAR MET pIRIR-IRPL), and other existing IRPL protocols, e.g., a low-temperature SAR MET pIRIR-IRPL (Kumar et al., 2021), or a pIR-IRPL (Duller et al., 2020), might lead to better or worse agreement with our IR-RF results.

Lastly, the DRC shape and signal saturation of the SAR IR-RF$_{70}$, IRPL and pIRIR signals of sample Gi326 were very similar (see Fig. 9), with field-saturation occurring below 85% or below 90% of the full saturation for the SAR and MAR protocols, respectively. This result aligns with the field-saturation of 84% reported by Buylaert et al. (2012b) for the IR-RF$_{RT}$ signal of a different sample. Failure to reach saturation even with a pIRIR$_{290}$ signal is in agreement with the findings of Yi et al. (2016) when using a high test dose (~500 Gy in their study and also here for the IRPL and pIRIR of sample Gi326). Although we report very similar IR-RF$_{70}$ DRC shapes for all but two samples (Fig. 8b, inset), we note that the aliquots used to obtain these curves are composed of hundreds of grains and previous single-grain investigations have pointed to a larger DRC shape variation, including for a sample also used in the present work (Sontag-González et al., 2024). The possibility of individual grains with an earlier or later-saturating IR-RF$_{70}$ DRC could explain the variability observed here for the multi-grain aliquots of some samples.

In comparison with the SAR DRC, the MAR IR-RF$_{70}$ DRC saturated slightly earlier: 85% of the signal intensity (relative to the signal at a dose of ~4000 Gy) was reached after a dose of ~1050 Gy, in contrast to ~1300 Gy in the SAR DRC. An earlier onset of saturation of the natural IR-RF$_{70}$ signal is also supported by a natural IR-RF$_{70}$ DRC built by Buchanan et al. (2022) using coarse-grain K-feldspar samples of known age from the Chinese Loess Plateau. Their natural DRC is not incompatible with our MAR DRC (Fig. S14a), though the high scatter in their data does not allow for a definitive comparison (c.f. Fig. S14b). Interestingly and contrary to our findings, in K-feldspar MET pIRIR studies, MAR approaches have performed better for old samples due to a later onset of saturation relative to SAR and allowed for D$_e$ values of up to ca. 1100–1200 Gy (e.g., Zhang et al., 2022; Liu et al., 2025) to be determined.

9 Conclusions

The IR-RF age underestimation for samples in the 200–300 Gy range reported by Buylaert et al. (2012b) was likely due to the measurement temperature (room temperature) and can be overcome by raising it to 70°C (i.e., IR-RF$_{70}$ SAR protocol). Based on our study, we recommend the following: (i) applying the vertical slide correction to account for sensitivity changes, (ii) using a natural dose curve segment length of several hundred Gy (e.g., 300 Gy) for sliding, and (iii) rejecting initial channels to mitigate the effects of the initial signal rise. Using these parameters, we observed an agreement with expected ages for four out of seven non-modern samples. However, two modern samples yielded slightly underestimated ages (ca. −2 ka). Furthermore, we propose implementing a sensitivity change test to identify samples unsuitable for IR-RF dating through the comparison of D$_e$ values obtained by using progressively higher-dose segments of the natural dose curve for sliding (see Fig. 10b). Although this procedure increases the measurement time, it might be a worthwhile addition until we better understand what causes the sensitivity changes during the first irradiation of some samples.

Our preliminary investigations using a MAR method suggest it holds promise, especially for samples with large sensitivity changes. However, since only six out of the nine samples of known age produced the expected D$_e$ values, we cannot yet recommend its routine application. In our approach, application of the MAR method only required the measurement of one additional aliquot per sample after the traditional SAR measurements.

For samples ranging from ~100−300 Gy, the mean D$_e$ values derived from the pIR$_{50}$IRPL$_{955}$ and the APh-IRPL$_{880}$ signals are in good agreement (at 2σ) with the expected doses, including two samples strongly overestimated with IR-RF$_{70}$. However, IR-RF$_{70}$ demonstrated better agreement than any of the IRPL signals for the two modern samples.

Finally, our study points to a similar upper limit of 1000–1300 Gy for both IR-RF and IRPL, despite the regenerative DRCs of both signals not reaching complete saturation. This finding supports the notion that both techniques target the same traps and indicates that there is some instability of the stored charges.

Acknowledgements

The authors thank Jan-Pieter Buylaert for access to data and samples used in a previous study (Buylaert et al., 2012b) and Bo Li for fruitful discussions. This study was supported by the German Research Foundation (MSG and M. Fuchs: DFG FU417/36-1; MKM and M. Fuchs: DFG FU417/19-1). MJ acknowledges European Research Council Advanced Grant - LUMIN (ERC-ADG-101097215) for supporting his contribution to this work. Mette Adrian and Vicki Hansen are thanked for sample preparation. Myungho Kook is thanked for technical support during the IRPL measurements.

Author contributions

MSG, MKM, M. Frouin and M. Fuchs designed the experiments and organized the inter-laboratory comparison. MSG and M. Frouin carried out IR-RF measurements. MSG and MJ carried out IRPL measurements. MSG analysed the results and prepared the manuscript with contributions from all authors. M. Fuchs obtained funding.

Data availability

550 The data analysed in this work is available at https://doi.org/10.5281/zenodo.14507179 (Sontag-González et al., 2025).

Competing interests

The authors declare that they have no conflict of interest.

References

555 Aitken, M. J.: An introduction to optical dating, Oxford University Press, 1998.

Ankjærgaard, C.: Exploring multiple-aliquot methods for quartz violet stimulated luminescence dating, Quat. Geochronol., 51, 99–109, https://doi.org/10.1016/j.quageo.2019.02.001, 2019.

Aubry, T., Dimuccio, L. A., Almeida, M., Buylaert, Fontana, L., Higham, T., Liard, M., Murray, A. S., Neves, M. J., Peyrouse, J.-B., and Walter, B.: Stratigraphic and technological evidence from the Middle Palaeolithic-
560 Châtelperronian-Aurignacian record at the Bordes-Fitte rockshelter (Roches d'Abilly site, Central France), J. Hum. Evol., 62, 116–137, https://doi.org/10.1016/j.jhevol.2011.10.009, 2012.

Autzen, M., Andersen, C. E., Bailey, M., and Murray, A. S.: Calibration quartz: An update on dose calculations for luminescence dating, Radiat. Meas., 157, 106828, https://doi.org/10.1016/j.radmeas.2022.106828, 2022.

Bøtter-Jensen, L., Thomsen, K. J., and Jain, M.: Review of optically stimulated luminescence (OSL) instrumental
565 developments for retrospective dosimetry, Radiat. Meas., 45, 253–257, https://doi.org/10.1016/j.radmeas.2009.11.030, 2010.

Buchanan, G. R., Tsukamoto, S., Zhang, J., and Long, H.: Testing the natural limits of infrared radiofluorescence dating of the Luochuan loess-palaeosol sequence, Chinese Loess Plateau, Radiat. Meas., 155, 106797, https://doi.org/10.1016/j.radmeas.2022.106797, 2022.

570 Buchanan, G. R., Tsukamoto, S., Zhang, J., and Long, H.: Testing infrared radiofluorescence dating on polymineral fine-grains from the Luochuan loess-palaeosol sequence, Chinese loess plateau, Quat. Geochronol., 79, 101485, https://doi.org/10.1016/j.quageo.2023.101485, 2024.

Buylaert, J.-P., Jain, M., Murray, A. S., Thomsen, K. J., Thiel, C., and Sohbati, R.: A robust feldspar luminescence dating method for Middle and Late Pleistocene sediments: Feldspar luminescence dating of Middle
575 and Late Pleistocene sediments, Boreas, 41, 435–451, https://doi.org/10.1111/j.1502-3885.2012.00248.x, 2012a.

Buylaert, J.-P., Jain, M., Murray, A. S., Thomsen, K. J., and Lapp, T.: IR-RF dating of sand-sized K-feldspar extracts: A test of accuracy, Radiat. Meas., 47, 759–765, https://doi.org/10.1016/j.radmeas.2012.06.021, 2012b.

Duller, G. A. T., Gunn, M., and Roberts, H. M.: Single grain infrared photoluminescence (IRPL) measurements of feldspars for dating, Radiat. Meas., 133, 106313, https://doi.org/10.1016/j.radmeas.2020.106313, 2020.

580 Duval, M., Guilarte, V., Campana, I., Arnold, L. J., Miguens, L., Iglesias, J., and Gonzalez-Sierra, S.: Quantifying hydrofluoric acid etching of quartz and feldspar coarse grains based on weight loss estimates: implication for ESR and luminescence dating studies, 36, 14, 2018.

Erfurt, G. and Krbetschek, M. R.: Studies on the physics of the infrared radioluminescence of potassium feldspar and on the methodology of its application to sediment dating, Radiat. Meas., 37, 505–510,
585 https://doi.org/10.1016/S1350-4487(03)00058-1, 2003.

Frouin, M., Huot, S., Mercier, N., Lahaye, C., and Lamothe, M.: The issue of laboratory bleaching in the infrared-radiofluorescence dating method, Radiat. Meas., 81, 212–217, https://doi.org/10.1016/j.radmeas.2014.12.012, 2015.

Frouin, M., Huot, S., Kreutzer, S., Lahaye, C., Lamothe, M., Philippe, A., and Mercier, N.: An improved
590 radiofluorescence single-aliquot regenerative dose protocol for K-feldspars, Quat. Geochronol., 38, 13–24, https://doi.org/10.1016/j.quageo.2016.11.004, 2017.

Huot, S., Frouin, M., and Lamothe, M.: Evidence of shallow TL peak contributions in infrared radiofluorescence, Radiat. Meas., 81, 237–241, https://doi.org/10.1016/j.radmeas.2015.05.009, 2015.

Hütt, G., Jaek, I., and Tchonka, J.: Optical dating: K-feldspars optical response stimulation spectra, Quat. Sci.
595 Rev., 7, 381–385, https://doi.org/10.1016/0277-3791(88)90033-9, 1988.

Key, A., Lauer, T., Skinner, M. M., Pope, M., Bridgland, D. R., Noble, L., and Proffitt, T.: On the earliest Acheulean in Britain: first dates and in-situ artefacts from the MIS 15 site of Fordwich (Kent, UK), R. Soc. Open Sci., 9, 211904, https://doi.org/10.1098/rsos.211904, 2022.

Kook, M., Kumar, R., Murray, A. S., Thomsen, K. J., and Jain, M.: Instrumentation for the non-destructive
600 optical measurement of trapped electrons in feldspar, Radiat. Meas., 120, 247–252, https://doi.org/10.1016/j.radmeas.2018.06.001, 2018.

Krbetschek, M. R., Trautmann, T., Dietrich, A., and Stolz, W.: Radioluminescence dating of sediments: methodological aspects, Radiat. Meas., 32, 493–498, https://doi.org/10.1016/S1350-4487(00)00122-0, 2000.

Kreutzer, S., Schmidt, C., Fuchs, M. C., Dietze, M., and Fuchs, M.: Introducing an R package for luminescence
605 dating analysis, Anc. TL, 30, 1–8, 2012.

Kreutzer, S., Murari, M. K., Frouin, M., Fuchs, M., and Mercier, N.: Always remain suspicious: a case study on tracking down a technical artefact while measuring IR-RF, Anc. TL, 35, 20–30, https://doi.org/10.26034/la.atl.2017.510, 2017.

Kreutzer, S., Mercier, N., and Lamothe, M.: Infrared-radiofluorescence: Dose saturation and long-term signal
610 stability of a K-feldspar sample, Radiat. Meas., 156, 106818, https://doi.org/10.1016/j.radmeas.2022.106818, 2022a.

Kreutzer, S., Burow, C., Dietze, M., Fuchs, M. C., Schmidt, C., Fischer, M., Friedrich, J., Mercier, N., Philippe, A., Riedesel, S., Autzen, M., Mittelstrass, D., Gray, H. J., and Galharret, J.-M.: Luminescence: Comprehensive Luminescence Dating Data Analysis v.0.9.19, 2022b.

615   Kumar, R., Kook, M., Murray, A. S., and Jain, M.: Towards direct measurement of electrons in metastable states in K-feldspar: Do infrared-photoluminescence and radioluminescence probe the same trap?, Radiat. Meas., 120, 7–13, https://doi.org/10.1016/j.radmeas.2018.06.018, 2018.

Kumar, R., Kook, M., and Jain, M.: Sediment dating using Infrared Photoluminescence, Quat. Geochronol., 62, 101147, https://doi.org/10.1016/j.quageo.2020.101147, 2021.

620   Lapp, T., Jain, M., Thomsen, K. J., Murray, A. S., and Buylaert, J.-P.: New luminescence measurement facilities in retrospective dosimetry, Radiat. Meas., 47, 803–808, https://doi.org/10.1016/j.radmeas.2012.02.006, 2012.

Li, B. and Li, S.-H.: Luminescence dating of K-feldspar from sediments: A protocol without anomalous fading correction, Quat. Geochronol., 6, 468–479, https://doi.org/10.1016/j.quageo.2011.05.001, 2011.

Li, B., Jacobs, Z., Roberts, R. G., and Li, S.-H.: Extending the age limit of luminescence dating using the dose-
625   dependent sensitivity of MET-pIRIR signals from K-feldspar, Quat. Geochronol., 17, 55–67, https://doi.org/10.1016/j.quageo.2013.02.003, 2013.

Liu, L., Yang, S., Li, P., Zhang, J., Li, R., Li, D., Xu, X., Luo, Y., and Yang, X.: First investigation of the luminescence dating of loess in the eastern Tibetan Plateau using K-feldspar MAR MET-pIRIR protocol, Quat. Geochronol., 86, 101648, https://doi.org/10.1016/j.quageo.2024.101648, 2025.

630   Lu, Y. C., Wang, X. L., and Wintle, A. G.: A new OSL chronology for dust accumulation in the last 130,000 yr for the Chinese Loess Plateau, Quat. Res., 67, 152–160, https://doi.org/10.1016/j.yqres.2006.08.003, 2007.

Madsen, A. T., Murray, A. S., and Andersen, T. J.: Optical Dating of Dune Ridges on Rømø, a Barrier Island in the Wadden Sea, Denmark, J. Coast. Res., 23, 1259–1269, https://doi.org/10.2112/05-0471.1, 2007.

Mittelstraß, D. and Kreutzer, S.: Spatially resolved infrared radiofluorescence: single-grain K-feldspar dating
635   using CCD imaging, Geochronology, 3, 299–319, https://doi.org/10.5194/gchron-3-299-2021, 2021.

Murari, M. K., Kreutzer, S., and Fuchs, M.: Further investigations on IR-RF: Dose recovery and correction, Radiat. Meas., 120, 110–119, https://doi.org/10.1016/j.radmeas.2018.04.017, 2018.

Murari, M. K., Kreutzer, S., Frouin, M., Friedrich, J., Lauer, T., Klasen, N., Schmidt, C., Tsukamoto, S., Richter, D., Mercier, N., and Fuchs, M.: Infrared Radiofluorescence (IR-RF) of K-Feldspar: An Interlaboratory
640   Comparison, Geochronometria, 48, 105–120, https://doi.org/10.2478/geochr-2021-0007, 2021.

Murray, A. S. and Funder, S.: Optically stimulated luminescence dating of a Danish Eemian coastal marine deposit: a test of accuracy, Quat. Sci. Rev., 22, 1177–1183, https://doi.org/10.1016/S0277-3791(03)00048-9, 2003.

Murray, A. S., Svendsen, J. I., Mangerud, J., and Astakhov, V. I.: Testing the accuracy of quartz OSL dating using a known-age Eemian site on the river Sula, northern Russia, Quat. Geochronol., 2, 102–109, https://doi.org/10.1016/j.quageo.2006.04.004, 2007.

Porat, N., Faerstein, G., Medialdea, A., and Murray, A. S.: Re-examination of common extraction and purification methods of quartz and feldspar for luminescence dating, Anc. TL, 33, 22–30, https://doi.org/10.26034/la.atl.2015.487, 2015.

Prasad, A. K., Poolton, N. R. J., Kook, M., and Jain, M.: Optical dating in a new light: A direct, non-destructive probe of trapped electrons, Sci. Rep., 7, 12097, https://doi.org/10.1038/s41598-017-10174-8, 2017.

R Core Team: R: A language and environment for statistical computing. R Foundation for Statistical Computing, Vienna, Austria, 2020.

Richter, D., Richter, A., and Dornich, K.: LEXSYG - A new system for luminescence research, Geochronometria, 40, 220–228, https://doi.org/10.2478/s13386-013-0110-0, 2013.

Scerri, E. M. L., Frouin, M., Breeze, P. S., Armitage, S. J., Candy, I., Groucutt, H. S., Drake, N., Parton, A., White, T. S., Alsharekh, A. M., and Petraglia, M. D.: The expansion of Acheulean hominins into the Nefud Desert of Arabia, Sci. Rep., 11, 10111, https://doi.org/10.1038/s41598-021-89489-6, 2021.

Sontag-González, M. and Fuchs, M.: Spectroscopic investigations of infrared-radiofluorescence (IR-RF) for equivalent dose estimation, Radiat. Meas., 153, 106733, https://doi.org/10.1016/j.radmeas.2022.106733, 2022.

Sontag-González, M., Mittelstraß, D., Kreutzer, S., and Fuchs, M.: Wavelength calibration and spectral sensitivity correction of luminescence measurements for dosimetry applications: Method comparison tested on the IR-RF of K-feldspar, Radiat. Meas., 159, 106876, https://doi.org/10.1016/j.radmeas.2022.106876, 2022.

Sontag-González, M., Kumar, R., Schwenninger, J.-L., Thieme, J., Kreutzer, S., and Frouin, M.: Short communication: Synchrotron-based elemental mapping of single grains to investigate variable infrared-radiofluorescence emissions for luminescence dating, Geochronology, 6, 77–88, https://doi.org/10.5194/gchron-6-77-2024, 2024.

Sontag-González, M., Murari, M. K., Jain, M., Frouin, M., and Fuchs, M.: Further investigations into the accuracy of infrared-radiofluorescence (IR-RF) and its inter-comparison with infrared photoluminescence (IRPL) dating (v1.0.1) [Data set]. Zenodo. https://doi.org/10.5281/zenodo.14507179, 2025.

Trautmann, T., Krbetschek, M. R., Dietrich, A., and Stolz, W.: Investigations of feldspar radioluminescence: potential for a new dating technique, Radiat. Meas., 29, 421–425, https://doi.org/10.1016/S1350-4487(98)00012-2, 1998.

Trautmann, T., Dietrich, A., Stolz, W., and Krbetschek, M. R.: Radioluminescence Dating: A New Tool for Quaternary Geology and Archaeology, Naturwissenschaften, 86, 441–444, https://doi.org/10.1007/s001140050649, 1999.

Trautmann, T., Krbetschek, M. R., and Stolz, W.: A systematic study of the radioluminescence properties of single feldspar grains, Radiat. Meas., 32, 685–690, https://doi.org/10.1016/S1350-4487(00)00077-9, 2000.

680   Varma, V., Biswas, R., and Singhvi, A.: Aspects of Infrared Radioluminescence dosimetry in K-feldspar, Geochronometria, 40, 266–273, https://doi.org/10.2478/s13386-013-0125-6, 2013.

Yi, S., Buylaert, J.-P., Murray, A. S., Lu, H., Thiel, C., and Zeng, L.: A detailed post-IR IRSL dating study of the Niuyangzigou loess site in northeastern China, Boreas, 45, 644–657, https://doi.org/10.1111/bor.12185, 2016.

Zhang, J., Hao, Q., and Li, S.-H.: An absolutely dated record of climate change over the last three glacial–interglacial cycles from Chinese loess deposits, Geology, 50, 1116–1120, https://doi.org/10.1130/G50125.1,
685   2022.
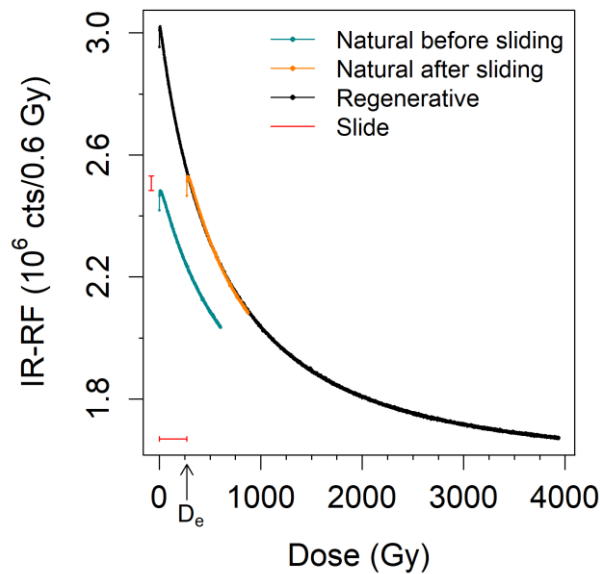
Figures

Figure 1: *IR-RF$_{70}$ measurements of one aliquot of sample 092202 (position 23) before and after vertical and horizontal sliding*
690   *of the natural dose curve (interference filter centred at 850 nm; FWHM of 40 nm). Note that the initial four channels (~2 Gy)*
were not considered for the assessment of sliding quality. The D$_e$ value determined for this aliquot is indicated on the x-axis.
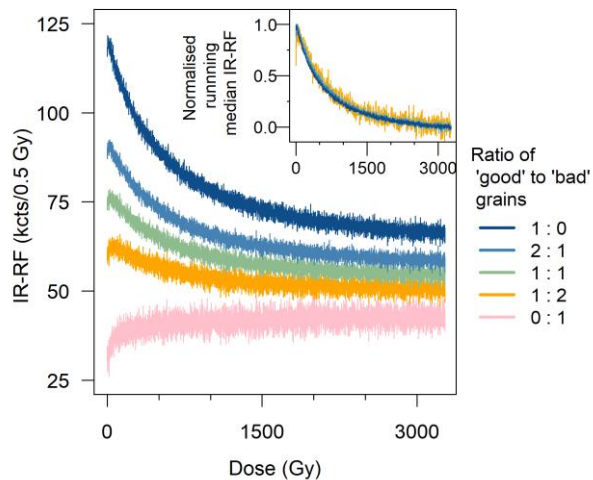
Figure 2: *Simulation of regenerative dose IR-RF$_{70}$ curves of aliquots of sample H22550 composed of a combination of grains with the expected IR-RF signal shape ('good' grains, Type #1) and grains with an initially increasing signal shape ('bad' grains, Type #2). The 'good' grain curve (dark blue) is the average of three individual grains with the expected signal shape, whereas the 'bad' grain curve was obtained from one grain. The grains are referred to as ID #3, #4, #5 and #6 in Sontag-González et al. (2024). The inset shows the same curves (except for that composed entirely of Type #2 grains) normalised to their maximum signal values, removing as background the median value of the last 100 channels (~60 Gy). Note the decrease in 'initial rise' with increasing proportion of 'good' grains relative to the total dynamic signal range.*
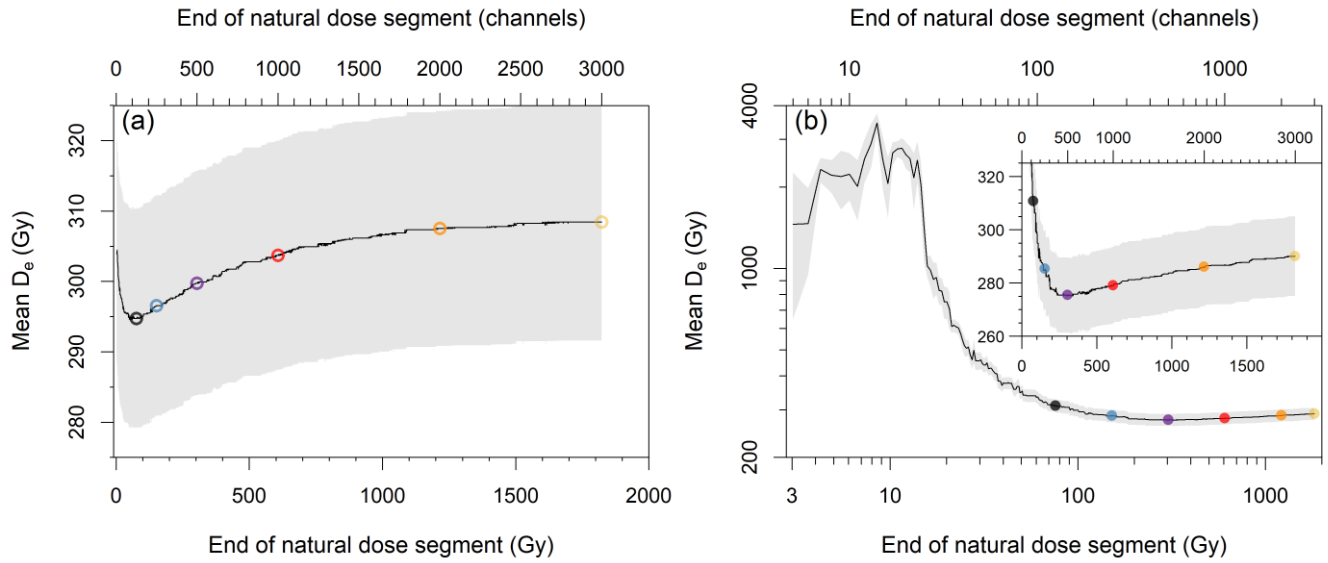
Figure 3: *Representative example of the effect of the length of the natural dose curve on the mean D_e for sample 981009 with an IR-RF$_{70}$ protocol (mean of 3 aliquots). The segment length was iteratively increased by one channel and D_e values estimated using (a) horizontal slide or (b) vertical and horizontal slide. The initial ~2 Gy (4 channels) were always rejected. Note that the main plot in panel (b) is shown in logarithmic scale. The inset shows a magnification of the region of interest of the main plot. The grey shading represents the standard error of the mean. The coloured points indicate the segment lengths chosen for further analysis.*
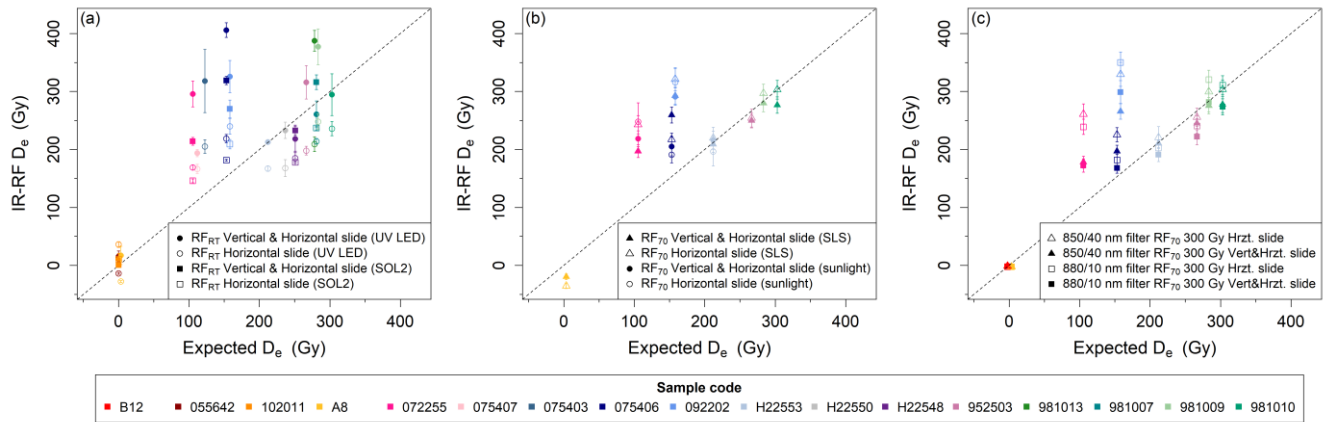
710 ***Figure 4:*** *Comparison of published and new IR-RF results with the expected D_e values. (a) IR-RF was measured at room temperature (RT). The measurements from Buylaert et al. (2012b) (open symbols) were analysed without vertical slide. Those measurements were re-analysed here with vertical slide correction of sensitivity changes (filled symbols). Aliquots were bleached with UV LEDs or an external solar simulator (SOL2) between the natural and regenerative dose measurements. (b) IR-RF of a subset of the same samples as in the previous panel measured at 70°C. D_e values were obtained with (filled symbols)*
715 *and without (open symbols) vertical slide. The same natural dose segments as in Buylaert et al. (2012b) were used for sliding. Aliquots were bleached with the internal solar simulator made up of an LED array (SLS; 9 samples) or direct sunlight (4 samples) between the natural and regenerative dose measurements. (c) All IR-RF_{70} with different detection filters using a segment of the natural dose curve spanning ~300 Gy (500 channels) but rejecting the initial ~2 Gy (4 channels). Note that a 5 Gy interval was placed between the expected doses of the modern samples to aid visualization.*

720
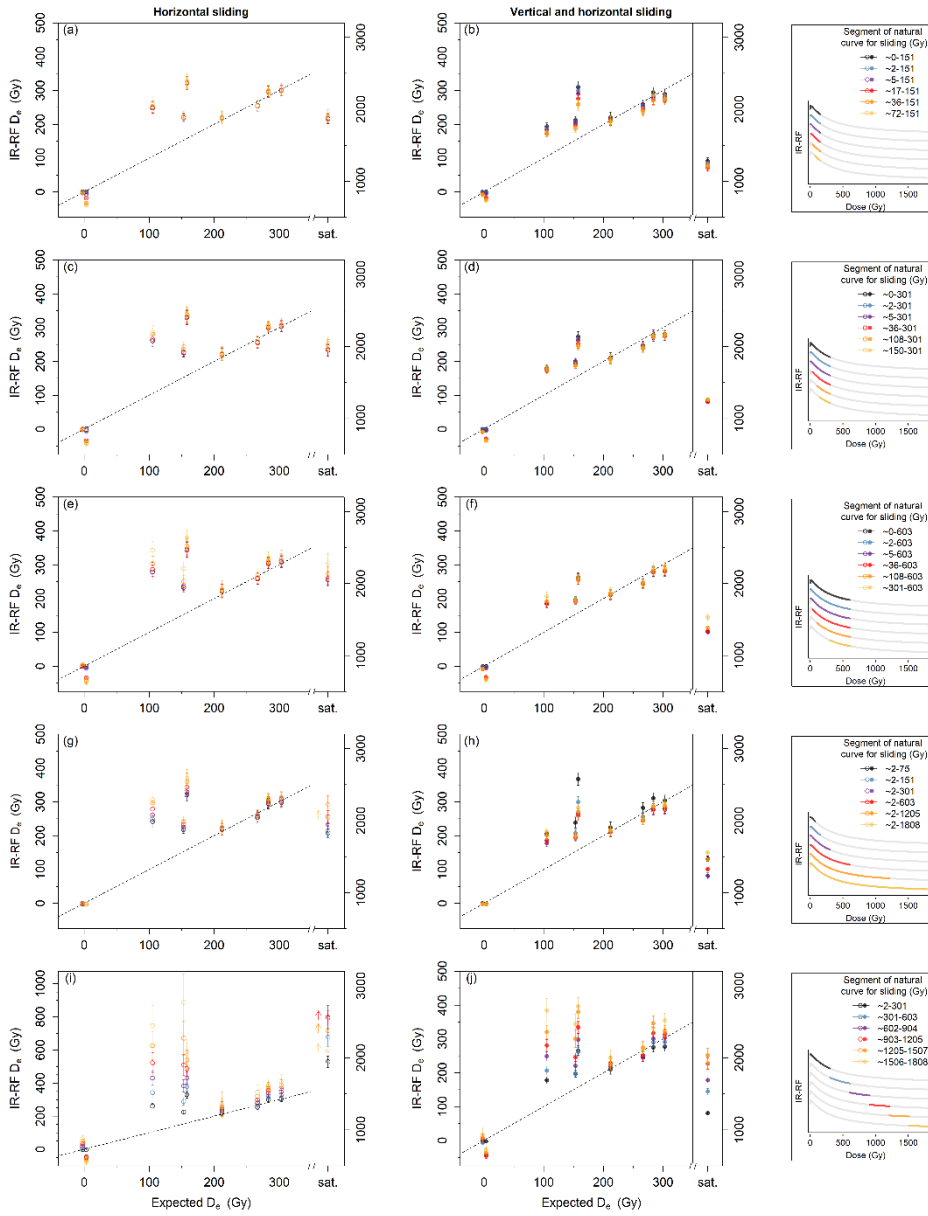
Figure 5: *Comparison of IR-RF$_{70}$ mean D_e values using fixed segments of the natural dose curve and (a, c, e, g, i) only horizontal sliding or (b, d, f, h, j) vertical and horizontal sliding. For clarity, the used segments of a representative natural dose curve (sample 092202) are shown in the legend box to the right of the corresponding plots. Note that a 5 Gy interval was placed between the expected doses of the two modern samples to aid visualization. The D_e for the field-saturated sample Gi326 is shown on the right-hand y-axis in each plot; its expected D_e is 'saturated' (sat.). The dashed line indicates the 1:1 line. (e, g) Arrows indicate a minimum estimate caused by the limit of the regenerative dose curve.*

730
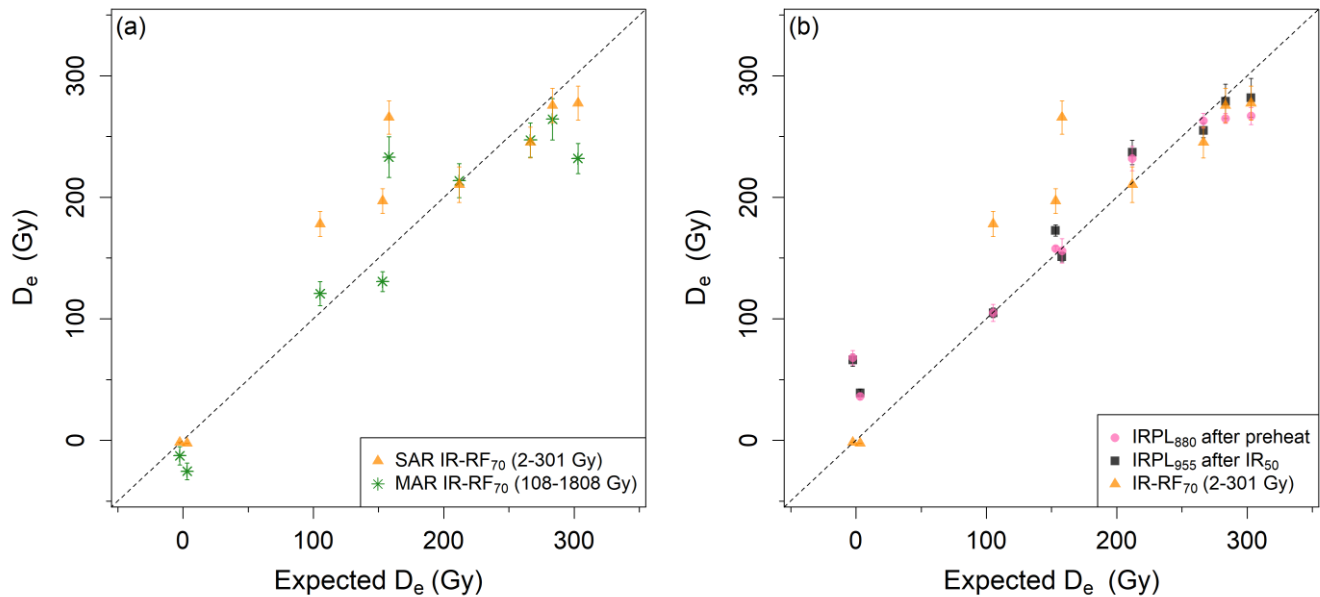
Figure 6: *Comparison of the new IR-RF$_{70}$ and IRPL results with the expected D$_e$ values. (a) Single-aliquot regenerative dose (SAR) IR-RF$_{70}$ results and those obtained using a multiple aliquot regenerative dose (MAR) protocol. Results are shown for the most reliable natural dose curve segment of each protocol, as given in the legend. (b) IRPL and SAR IR-RF$_{70}$ measured on of the same set of samples. The IRPL D$_e$ are a combination of new measurements and those from Kumar et al. (2021). The*

735 *subscript after 'IRPL' in the legend indicates the wavelength of the targeted emission. IR-RF$_{70}$ D$_e$ values were obtained with vertical and horizontal slide. Note that a 5 Gy interval was placed between the expected doses of the modern samples to aid visualization.*
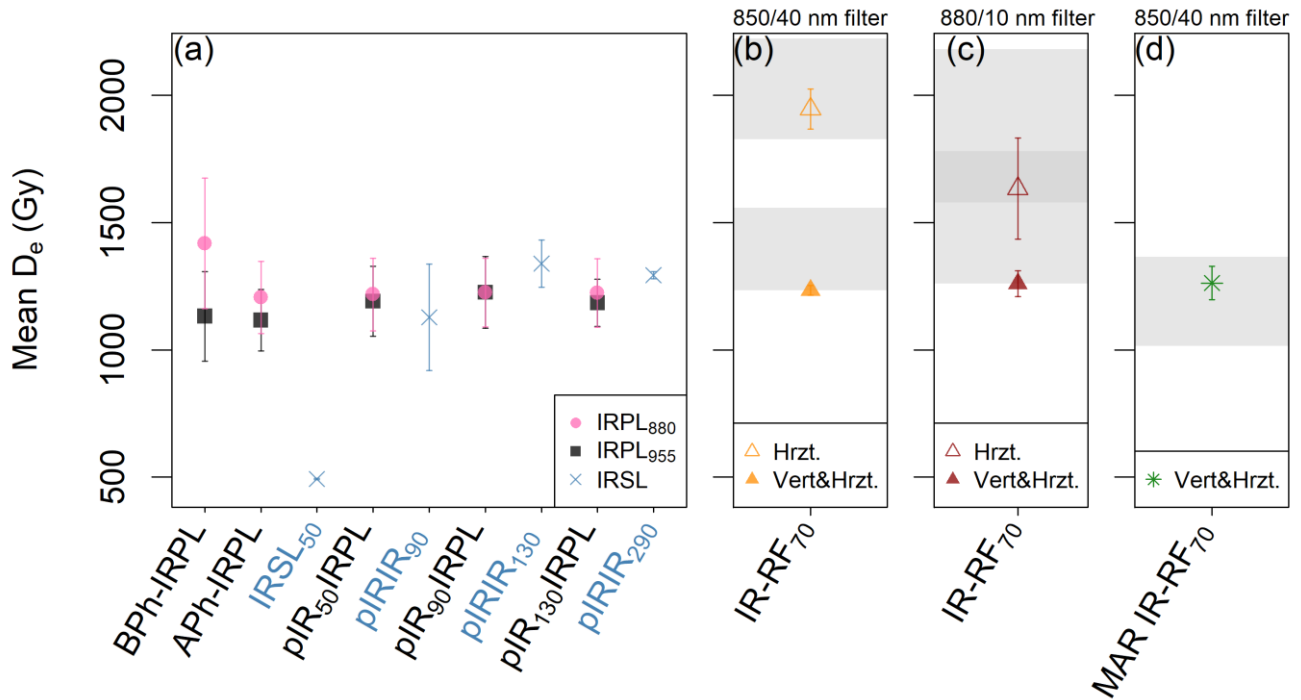
740 ***Figure 7:*** *Comparison at field-saturation for sample Gi326. (a) Mean D_e values obtained from the various steps in the IRPL sequence, including the IRSL steps (highlighted in blue in the x-axis labels). 'BPh' and 'APh' refer to before and after the preheat step, respectively. The IR-RF mean D_e values were obtained using (b, d) an 850/40 nm and (c) an 880/10 nm bandpass filter. (b, c) The initial ~300 Gy segment of the natural dose curve (rejecting the first ~2 Gy) was used with horizontal or with vertical and horizontal sliding (Hrzt. and Vert&Hrzt., respectively). (d) Results obtained using a multiple aliquot regenerative*

745 *dose (MAR) protocol and sliding the natural dose curve segment spanning 108−1808 Gy. The range of D_e values that could be obtained using alternative natural dose curve segments (i.e., those in (b) Fig. 5g–h, (c) Fig. S8g–h and (d) Fig. S10b–d) are shown as grey bands without the associated uncertainties.*
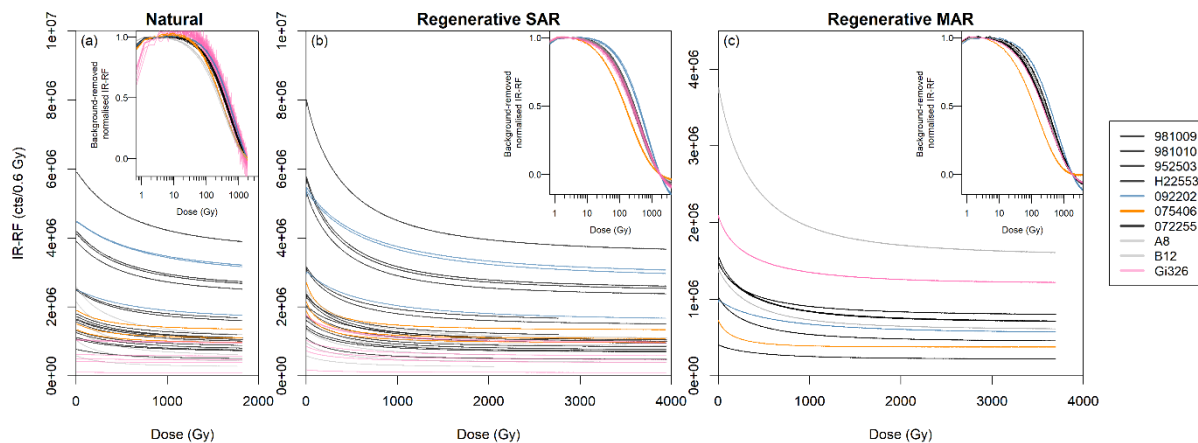
Figure 8: *IR-RF DRC shape comparison of (a) the natural, (b) the regenerative dose signal using a SAR and (c) the regenerative dose signal using a MAR protocol; all measured with an 850 nm bandpass filter (FWHM: 40 nm). In the insets, a background was subtracted from the IR-RF curves, corresponding to the signal value at a dose of 1800 Gy before normalisation to the signal value at 3 Gy. Curves from the two modern samples and the field-saturated sample are shown in pink and grey, respectively. The DRCs of two additional samples are coloured to highlight their deviation from the curve shape of all other samples.*
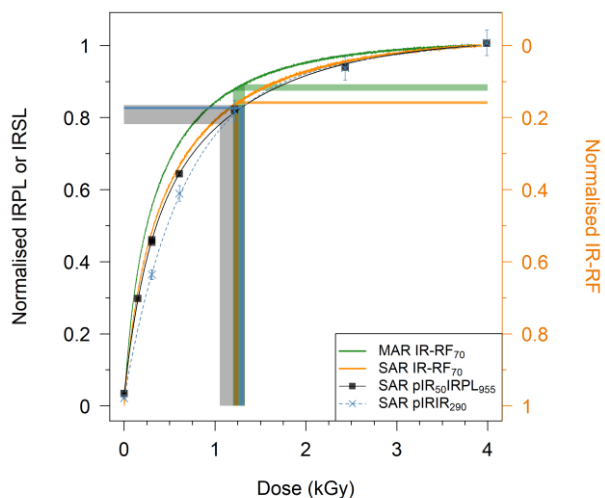
Figure 9: *DRC shape comparison of representative aliquots of Gi326. The pIR$_{50}$IRPL$_{955}$ and the pIR$_{90}$IR$_{290}$ curves are double*
exponential functions fitted to the sensitivity corrected signals (L$_x$/T$_x$) of 7–8 regenerative doses each, including a repeated
dose point (~300 Gy). All curves were normalised to their maximum values. Before normalisation, a background was
subtracted from the IR-RF curves, corresponding to the median value of the last 100 channels (~60 Gy). The IR-RF curves
decrease with dose, so they were plotted on an inverted axis (right-hand side) to allow for a direct comparison. The shaded
regions indicate the 1σ range around the four mean D$_e$ values and their projection onto the corresponding DRC.
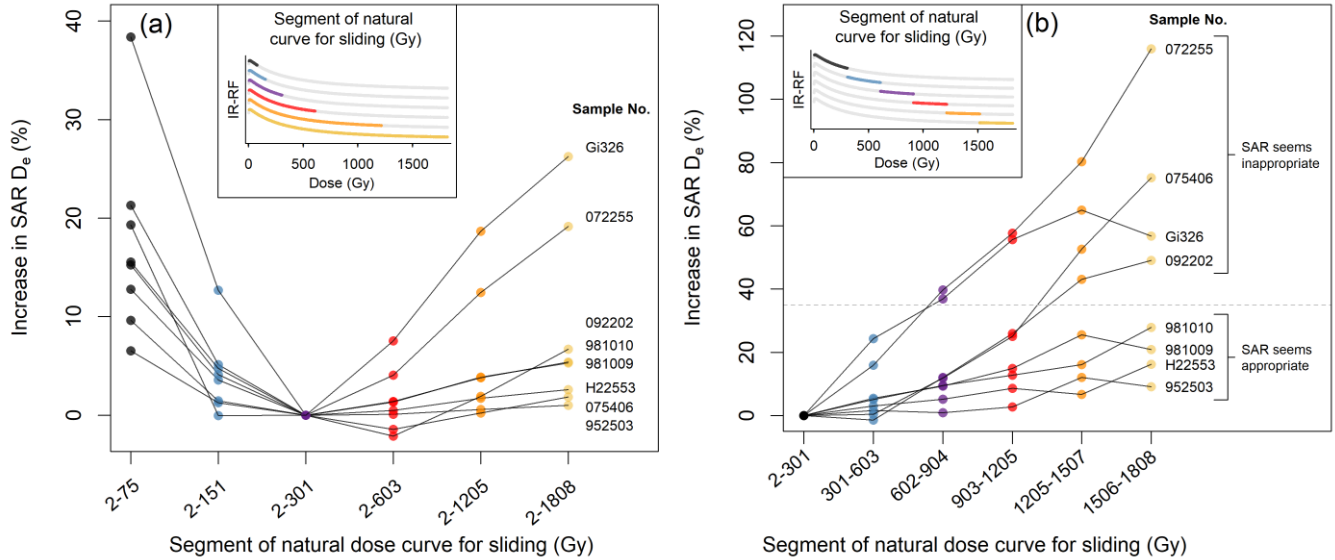
Figure 10: *Test of progressive sensitivity changes during the IR-RF$_{70}$ natural dose curve measurement. D$_e$ values of non-modern samples were obtained using fixed segments of the natural dose curve according to the x-axis labels with vertical and horizontal sliding (same data and colours as in (a) Fig. 5h and (b) Fig. 5j). The increase in D$_e$ is relative to that obtained from the segment 2−301 Gy. (b) The dashed line (35% increase) separates samples that produce D$_e$ values within 2σ of the expected dose and those that do not.*

 Tables

Table 1: Details on sampling locations and previous dating studies. Uncertainties in the expected ages represent one standard error. IR-RF$_{RT}$ refers to the room temperature measurement protocol. Previous IR-RF$_{RT}$, IR-RF$_{70}$ and IRPL ages are given in Buylaert et al. (2012b), Murari et al. (2021) and Kumar et al. (2021), respectively.

Code	Site & Location	Sediment type	Grain size (µm)	Expected Age (ka)	Type of age control	Previous IR-RF or IRPL studies
981007	Gammelmark (Denmark)	coastal marine sand	150–250	130±2	Biostratigraphy and quartz OSL (Murray and Funder, 2003; Buylaert et al., 2012a)	IR-RF$_{RT}$
981009			150–250	130±2		IR-RF$_{RT}$, IRPL
981010			150–250	130±2		IR-RF$_{RT}$, IRPL
981013			90–150	130±2		IR-RF$_{RT}$, IRPL
952503	Sula (Russia)	coastal marine sand	150–212	130±2	Biostratigraphy and quartz OSL (Murray et al., 2007; Buylaert et al., 2012a)	IR-RF$_{RT}$, IRPL
H22548			180–250	130±2		IR-RF$_{RT}$
H22550			180–250	130±2		IR-RF$_{RT}$
H22553			180–250	130±2		IR-RF$_{RT}$, IRPL
092202	Indre-et-Loire (France)	colluvium	180–250	45.5±2.5	^{14}C (Aubry et al., 2012)	IR-RF$_{RT}$, IRPL
075403	Sinai peninsula (Egypt)	reworked dune sand	180–250	37±4*		IR-RF$_{RT}$
075406			180–250	41±4*		IR-RF$_{RT}$
075407			180–250	40±4*		IR-RF$_{RT}$, IRPL
072255	Carregueira (Portugal)	eolian sand	180–250	21.9±2.2*	Quartz OSL (Buylaert et al., 2012a)	IR-RF$_{RT}$, IRPL
055642	North Jutland (Denmark)	beach sand	90–180	-0.0008±0.0018*		IR-RF$_{RT}$
102011	Maria Pia Beach (Sardinia)	beach sand	180–250	-0.001±0.010*		IR-RF$_{RT}$
A8	Dune, Rømø (Denmark)	eolian dune sand	180–250	0.41±0.05*	Quartz OSL (Madsen et al., 2007)	IR-RF$_{RT}$
B12	Wadden Sea (Denmark)	coastal marine deposits	180–250	0.01±0.002*		IRPL
Gi326	Bayreuth (Germany)	Triassic sandstone	90–200	~250 Ma	Lithostratigraphy (Murari et al., 2021)	IR-RF$_{70}$

* Ages corrected by 8.25% (Autzen et al., 2022).

 Table 2: IR-RF measurement protocols. 'Natural dose' curve (step 2) refers to the RF measurement where an additive dose is administered on top of the natural dose. The length of the 'regenerative dose' measurements (step 6) was sometimes shortened for younger samples.

Step	IR-RF$_{RT}$ SAR protocol (Buylaert et al., 2012b)	IR-RF$_{70}$ SAR protocol	IR-RF$_{70}$ MAR protocol Natural (same as SAR)	Regenerative	Purpose
1	-	Preheat at 70°C for 900 s	Preheat at 70°C for 900 s	-	Stabilise temperature
2	RF at room temperature for between ~9 Gy and ~480 Gy	RF at 70°C for 30 000 s (~1800 Gy)*	RF at 70°C for 30 000 s (~1800 Gy)*	-	Obtain 'natural dose' curve
3	UV bleach for 1500 s or Hönle SOL2 bleaching for 14 400 s	'Solar simulator' bleaching for 24 817 s	'Solar simulator' bleaching for 24 817 s	'Solar simulator' bleaching for 24 817 s	Fully remove signal
4	Pause for at least 1 h	Pause for 2 h	Pause for 2 h	Pause for 2 h	Reduce phosphorescence
5	-	Preheat at 70°C for 900 s	Preheat at 70°C for 900 s	Preheat at 70°C for 900 s	Stabilise temperature
6	RF at room temperature for between ~350 Gy and ~2940 Gy	RF at 70°C for between 35 000 and 65 000 s (~2100–3900 Gy)	RF at 70°C (at least one channel)	RF at 70°C for 65 000 s (~3900 Gy)	Obtain 'regenerative dose' curve

* Only a segment of the natural dose curve was used for final D_e estimation, see section 4.4.

785 ***Table 3:*** *Results from IR-RF measurements at room temperature (RT) either with or without sensitivity change correction. Data has been re-analysed from Buylaert et al. (2012b). Aliquots were bleached with UV LEDs or an external solar simulator (SOL2) between the natural and regenerative dose steps. 'n' refers to the number of aliquots used to determine the arithmetic mean D_e. IR-RF D_e uncertainties represent the standard error.*

Sample code	Expected D_e (Gy)	IR-RF$_{RT}$ (UV LED bleach)			IR-RF$_{RT}$ (SOL2 bleach)		
		n	Horizontal slide D_e (Gy)	Vertical and horizontal slide D_e (Gy)	n	Horizontal slide D_e (Gy)	Vertical and horizontal slide D_e (Gy)
981007	280.8±11.3	6	214.0±4.9	260.7±23.0	4	236.9±3.4	316.0±12.7
981009	283.4±11.3	11	247.9±13.5	377.2±30.9	-	-	-
981010	302.9±12.6	4	235.9±12.2	294.5±36.1	-	-	-
981013	278.2±12.5	5	209.1±12.9	387.5±17.9	-	-	-
952503	266.5±12.4	11	198.0±7.4	315.9±28.9	-	-	-
H22548	250.9±9.9	5	185.1±12.0	218.4±23.7	4	178.1±1.4	232.7±7.6
H22550	236.6±11.0	10	167.7±14.6	233.0±14.1	-	-	-
H22553	211.9±10.9	3	167.0±4.5	212.6±3.6	-	-	-
092202	157.9±10.5	13	239.7±13.3	325.8±27.8	4	209.2±8.1	270.0±15.2
075403	122.6±13.4	6	205.1±11.6	318.2±54.4	-	-	-
075406	153.0±16.4	9	218.7±7.2	405.9±12.7	4	181.6±1.5	319.1±7.1
075407	111.7±11.9	3	166.5±7.9	193.9±6.2	-	-	-
072255	105.2±11.4	15	169.1±4.4	295.7±22.3	4	146.0±3.3	214.0±6.9
055642	-0.002±-0.004	6	-13.6±1.6	15.5±9.3	-	-	-
102011	-0.01±0.01	8	36.2±4.9	10.6±2.4	4	10.5±10.5	0.6±1.5
A8	0.69±0.08	6	-27.8±1.5	17.4±15.7	-	-	-

790   **Table 4:** *Results from IR-RF measurements at 70°C using different bandpass filters and IRPL measurements after the preheat step (APh) and after the $IRSL_{50}$ step ($pIR_{50}IRPL$). IR-RF D_e values were obtained using either a single or multiple aliquot regenerative dose (SAR or MAR, respectively) procedure. SAR IR-RF D_e values were obtained using the initial ~300 Gy (500 channels) of the natural dose curve, rejecting the initial ~2 Gy (4 channels) and applying a sensitivity change correction (horizontal and vertical slide), whereas MAR D_e values were obtained from segments of the natural dose curve spanning ca. 108−1808 Gy (180−3000 channels). IRPL measurements marked with an asterisk are taken from Kumar et al. (2021). 'n' refers to the number of aliquots used to determine the arithmetic mean D_e. IR-RF D_e uncertainties represent the standard error.*

| Sample code | Expected D_e (Gy) | IR-RF$_{70}$ | | | | | IRPL | | | | |
| | | 850/40 nm filter | | | 880/10 nm filter | | | IRPL$_{880}$ D_e (Gy) | | IRPL$_{955}$ D_e (Gy) | |
		n	SAR D_e (Gy)	MAR D_e (Gy)	n	SAR D_e (Gy)	n	APh	pIR$_{50}$IRPL	APh	pIR$_{50}$IRPL
981009	283.4±11.3	4	275.5±14.1	264.3±17.1	3	281.8±16.9	3*	265±4	297±9	226±3	279±14
981010	302.9±12.6	3	277.5±14.1	232.0±12.4	3	273.5±14.0	3*	267±7	280±5	246±9	282±16
952503	266.5±12.4	3	245.1±12.7	247.1±14.2	3	222.1±14.1	6*	263±6	288±7	226±8	255±6
H22553	211.9±10.9	3	210.5±14.7	213.6±14.0	3	191.2±12.0	3*	232±10	248±11	205±10	237±10
092202	157.9±10.5	3	265.8±13.7	233.0±16.7	3	298.9±19.9	3*	156±10	159±11	146±3	151±4
075406	153.0±16.4	3	197.0±10.1	130.6±8.2	3	168.0±8.8	4	158±2	176±4	139±3	173±5
072255	105.2±11.4	3	178.1±10.3	120.7±9.9	3	172.5±11.6	3*	105±7	103±6	94±2	105±4
A8	0.69±0.08	3	-2.4±-0.6	−25.6±6.9	3	-2.2±-0.6	7	36±3	41±3	24±2	39±3
B12	0.01±0.01	3	-1.8±-0.6	−12.7±7.6	3	-1.6±-0.6	3*	68±6	70±4	39±1	66±5
Gi326	~500 000	6	1234±19	1263±65	5	1260±51	3	1206±141	1217±143	1116±120	1191±138